

# Evolution of spatially resolved star formation main sequence and surface density profiles in massive disc galaxies at $0 \lesssim z \lesssim 1$ : inside-out stellar mass buildup and quenching

Abdurro'uf<sup>1</sup><sup>★</sup> and Masayuki Akiyama<sup>1</sup>

<sup>1</sup>*Astronomical Institute, Tohoku University, Aramaki, Aoba, Sendai 980-8578, Japan*

Accepted XXX. Received YYY; in original form ZZZ

## ABSTRACT

We investigate a relation between sub-galactic surface densities (at a  $\sim 1$  kpc scale) of star formation rate (SFR) and stellar mass ( $M_*$ ) namely spatially resolved star formation main sequence (SFMS) at  $z \sim 0$  and  $z \sim 1$  of massive ( $\log(M_*/M_\odot) > 10.5$ ) face-on disc galaxies and examine the evolution of the relation with cosmic time. The spatially resolved SFMS of  $z \sim 0$  galaxies is discussed in a companion paper. For  $z \sim 1$  sample, we use 8 bands imaging dataset from CANDELS and 3D-HST which provides a rest-frame FUV-NIR spectral energy distribution (SED) for galaxies at  $0.8 \lesssim z \lesssim 1.8$ . We perform a pixel-to-pixel SED fitting to derive the spatially resolved SFR and  $M_*$  distributions in a galaxy. We find a linear spatially resolved SFMS in the  $z \sim 1$  galaxies that lie within  $\pm 0.3$  dex from the global SFMS, while a "flattening" at high  $\Sigma_*$  end is found in the spatially resolved SFMS of the galaxies that lie below  $-0.3$  dex from the global SFMS. The "flattening" trend is consistent with a decline of the sSFR radial profile (sSFR( $r$ )) in the central region of the corresponding galaxies. Comparison with the spatially resolved SFMS in the  $z \sim 0$  galaxies shows smaller difference in the sSFR at low  $\Sigma_*$  ( $\sim 0.4$  dex at  $\log(\Sigma_*[M_\odot \text{kpc}^{-2}]) = 7.0$ ) than that at high  $\Sigma_*$  ( $\sim 1.5$  dex at  $\log(\Sigma_*[M_\odot \text{kpc}^{-2}]) = 8.5$ ). This trend is consistent with the evolution of the sSFR( $r$ ) radial profile, which shows a faster decrease in the central region than in the outskirt, agrees with the inside-out quenching scenario. We then derive an empirical model for the evolution of the  $\Sigma_*(r)$ ,  $\Sigma_{\text{SFR}}(r)$  and sSFR( $r$ ) radial profiles. Based on the empirical model, we estimate the radial profile of the quenching timescale and reproduce the observed spatially resolved SFMS at  $z \sim 1$  and  $z \sim 0$ .

**Key words:** galaxies: evolution – galaxies: formation – galaxies: fundamental parameters – galaxies: structure – galaxies: star formation – galaxies: spiral.

## 1 INTRODUCTION

Thanks to an increasing number of wide-field and multi-wavelength imaging dataset, we can study scaling relations of galaxies in a wide redshift range. Investigation on properties of galaxies found that there is a linear correlation between the integrated star formation rate (SFR) and stellar mass ( $M_*$ ) of star-forming galaxies namely star formation main sequence (SFMS) (e.g. Brinchmann et al. 2004; Daddi et al. 2007; Elbaz et al. 2007; Noeske et al. 2007; Salim et al. 2007; Whitaker et al. 2012; Speagle et al. 2014). The integrated SFMS relation suggests that SFR increases with  $M_*$  as a power law ( $\text{SFR} \propto M_*^\alpha$  with  $\alpha \sim 1$ ) over at least two

orders of magnitude in stellar mass ( $\sim 10^9 - 10^{11} M_\odot$ ) up to  $z \sim 6$ . The normalization of the integrated SFMS relation shows a factor of  $\sim 2$  dex decrease from  $z \sim 6$  to  $z \sim 0$  (Speagle et al. 2014). Tightness of the integrated SFMS relation,  $1\sigma$  scatter of only  $\sim 0.3$  dex in the redshift range of  $0 \lesssim z \lesssim 3$  (e.g. Whitaker et al. 2012; Speagle et al. 2014; Kurczynski et al. 2016), implies an importance of a continuous internal secular process in driving the star formation activity of the majority of galaxies rather than stochastic merger process (Noeske et al. 2007).

Star-forming galaxies are evolving with cosmic time maintaining their position within about  $\pm 0.3$  dex around the global SFMS. Once the star formation activity in a galaxy is quenched, the galaxy will move away from the global SFMS relation until it reaches red-sequence which is populated by

<sup>★</sup> E-mail: abdurrouf@astr.tohoku.ac.jp

quiescent galaxies. Responsible mechanisms for the quenching process are still unclear. Several quenching mechanisms have been proposed. Rapid gas consumption by starburst event can make galaxies to run out their gas and in combination with the outflow driven by a stellar feedback can quench star formation in the galaxies (e.g. Murray et al. 2005). Furthermore, feedback from a central super massive black hole growth process (i.e. AGN feedback) can suppress the cold gas supply to galaxies through quasar or radio feedback mode (e.g. Sanders et al. 1988; Silk & Rees 1998; Springel et al. 2005; Hopkins et al. 2006, 2008; Schawinski et al. 2006; Fabian 2012). On the other hand, morphological quenching scenario proposes that once central spheroidal component (i.e. bulge) is formed, the deeper gravitational potential of the bulge can stabilize gas in the disc, and the stabilization prevents gas collapse and stop the star formation in the disc (e.g. Martig et al. 2009; Genzel et al. 2014). The suppression of cold gas accretion into a galaxy will also happen once the growth of host dark matter halo mass reaches a certain critical mass ( $\sim 10^{12} M_{\odot}$ ) above which newly accreted gas will be shock heated (e.g. Birnboim & Dekel 2003; Dekel & Birnboim 2006).

Investigation on the morphology and structural properties of star-forming and quiescent galaxies revealed that quiescent galaxies tend to have higher Sérsic index ( $n$ ) and concentration index, i.e. higher bulge fraction (B/T, bulge to total mass ratio), than star-forming galaxies (e.g. Kauffmann et al. 2003; Wuyts et al. 2011). It is still unclear how galaxies change their morphology from disc-dominated (low concentration index and sersic index,  $n \sim 1$ ) to bulge-dominated (high concentration index and sersic index,  $n \gtrsim 3$ ). Investigation on the radial stellar mass surface density profiles of massive galaxies at  $0 \lesssim z \lesssim 3$  revealed that massive galaxies establish their structures and stellar masses in a "inside-to-outside" manner, where a bulge is already formed at  $z \sim 2$  then a disc component is build subsequently (e.g. van Dokkum et al. 2010; Förster Schreiber et al. 2011; Nelson et al. 2012, 2016; Patel et al. 2013; Morishita et al. 2015; Tacchella et al. 2015; Tadaki et al. 2017). Although it is suggested that galaxies change their morphologies to a bulge-dominated system during the quenching process, other investigation suggests that quiescent galaxies were born as a bulge-dominated system (Abramson & Morishita 2016).

As the stellar mass buildup progresses inside-out, the quenching process also happen in the similar manner. This "inside-out quenching" process is imprinted in the positive gradient of sSFR radial profile of massive galaxies at  $0 \lesssim z \lesssim 2$  (e.g. Tacchella et al. 2015, 2017; González Delgado et al. 2016; Abdurro'uf & Akiyama 2017). It is still unclear what is physical mechanism responsible for the inside-out quenching. Some simulation works have been done to study the physical mechanism behind the inside-out quenching. Cosmological zoom-in simulations done by Zolotov et al. (2015) and Tacchella et al. (2016a,b) suggest that galaxy may experience central gas compaction followed by the central starburst which consume gas rapidly in the central region. If further cold gas supply into the central region is stopped due to radiative stellar feedback and/or AGN feedback, the onset of the inside-out quenching begin.

To understand how galaxy's internal star formation leads to the building up of the galaxy's stellar mass and structure and also to understand how an internal quenching

process shut down the star formation in the galaxy, an analysis on the spatially resolved distributions of  $M_*$  and SFR for a large number of galaxies in a wide redshift range is essential. Recently, investigations on sub-galactic ( $\sim 1$  kpc-scale) surface densities of stellar mass ( $\Sigma_*$ ) and SFR ( $\Sigma_{\text{SFR}}$ ) of  $z \sim 0$  and  $z \sim 1$  galaxies revealed that there is a nearly linear relation, in the logarithmic scale, between  $\Sigma_*$  and  $\Sigma_{\text{SFR}}$  in a similar form as found in the integrated scaling relation, namely spatially resolved SFMS relation (for  $z \sim 1$ : Wuyts et al. (2013) and Magdis et al. (2016) and for  $z \sim 0$ : Cano-Díaz et al. (2016), Maragkoudakis et al. (2017) and Abdurro'uf & Akiyama (2017)). Currently, the spatially resolved SFMS relations are studied with different methods which cause discrepancies in term of the measured slope and zero point. Cano-Díaz et al. (2016) reported a slope of 0.72 and zero point of  $-7.95$ , while the other four papers reported a steeper slope close to unity with a zero point of  $\sim -8.3$  (Wuyts et al. (2013) and Magdis et al. (2016)),  $-9.01$  (Maragkoudakis et al. 2017) and  $-9.58$  (Abdurro'uf & Akiyama 2017). The  $z \sim 1$  relations (Wuyts et al. 2013; Magdis et al. 2016) seem to agree with each other, while the  $z \sim 0$  relations (Cano-Díaz et al. 2016; Maragkoudakis et al. 2017; Abdurro'uf & Akiyama 2017) show discrepancy. In the same way, it is suggested for the integrated SFMS by Speagle et al. (2014) that the differences in slope and zero point are caused by differences in the applied SFR indicators (i.e. method to derive SFR), initial mass function (IMF), stellar population synthesis model and sample selection, the difference in the spatially resolved SFMS relations could be caused by the difference in methodology, especially the methodology to derive the spatially resolved  $\Sigma_{\text{SFR}}$ .

Understanding the spatially resolved SFMS relation and its evolution with cosmic time is very important to study the origin of the global SFMS relation, because the sub-galactic relation can be a more fundamental relation from which the global relation is originated. Abdurro'uf & Akiyama (2017) studied the spatially resolved SFMS relation in the local ( $0.01 < z < 0.02$ ) massive ( $M_* > 10^{10.5} M_{\odot}$ ) disc galaxies using seven bands (FUV, NUV,  $u$ ,  $g$ ,  $r$ ,  $i$  and  $z$ ) imaging data from Galaxy Evolution Explorer (GALEX) and Sloan Digital Sky Survey (SDSS). We derived the spatially resolved SFR and stellar mass of a galaxy by using a method so-called pixel-to-pixel spectral energy distribution (SED) fitting which fits the spatially resolved SED of a galaxy with a set of model photometric SEDs using a Bayesian statistics approach. The reason for choosing the method is that the same method is applicable to a large number of galaxies even at high redshifts, thanks to the high spatial resolution of the NIR images taken by the Hubble Space Telescope (HST).

Abdurro'uf & Akiyama (2017) found that the spatially resolved SFMS in the local massive disc galaxies show that  $\Sigma_{\text{SFR}}$  increases linearly with  $\Sigma_*$  at low  $\Sigma_*$  ( $\lesssim 10^{7.5} M_{\odot} \text{kpc}^{-2}$ ) range, while flattened at high  $\Sigma_*$  ( $\gtrsim 10^{7.5} M_{\odot} \text{kpc}^{-2}$ ) range. Investigation on the spatially resolved SFMS relation in the galaxies above  $+0.3$  dex (hereafter, z0-AMS1), between  $-0.3$  and  $+0.3$  dex (hereafter, z0-AMS2) and below  $-0.3$  dex (hereafter z0-AMS3) of the global SFMS relation, found a tight spatially resolved SFMS relation in the z0-AMS1 and z0-AMS2 galaxies, while the relation seems to be broken in the z0-AMS3 galaxies. The normalization in the global SFMS in each group is preserved in the spatially resolved SFMS, in the sense that the spatially resolved SFMS of z0-AMS1

galaxies has higher normalization than the spatially resolved SFMS of z0-AMS2 galaxies.

In the current work, we extend our previous study of the spatially resolved SFMS to massive disc galaxies at  $0.8 < z < 1.8$  using the similar pixel-to-pixel SED fitting method applied to the 8 bands (F435W, F606W, F775W, F814W, F850LP, F125W, F140W and F160W) imaging data from the Cosmic Assembly Near-infrared Deep Extragalactic Legacy Survey (CANDELS; Grogin et al. 2011; Koekemoer et al. 2011) and 3D-HST (Brammer et al. 2012) projects. Similar rest-frame wavelength coverage (FUV-NIR) and spatial resolution ( $\sim 1$  kpc) of the imaging data used in this work and the previous work allows a consistent comparison and could resolve the problem caused by the different method in studying the spatially resolved SFMS at different redshifts. Furthermore, we also discuss about the evolution of the  $\Sigma_*$ ,  $\Sigma_{\text{SFR}}$  and sSFR radial profiles.

The structure of this paper is as follows. In Section 2, we explain the sample. Section 3 presents our methodology, pixel-to-pixel SED fitting. Results and discussions are presented in Section 4 and 5, respectively. The cosmological parameters of  $\Omega_m = 0.3$ ,  $\Omega_\Lambda = 0.7$  and  $H_0 = 70 \text{ km s}^{-1} \text{ Mpc}^{-1}$  are used throughout this paper. We use  $M_*$  to represent the total stellar mass of a galaxy, while  $m_*$  is used to represent the stellar mass within a sub-galactic region. Terms global is used to indicate a galaxy-scale quantity, while term sub-galactic is used to represent  $\sim 1$  kpc scale quantity within a galaxy.

## 2 DATA SAMPLE

To examine the relation between  $\Sigma_*$  and  $\Sigma_{\text{SFR}}$  of galaxies at  $z \sim 1$  with the same resolution of 1-2 kpc as those of local galaxies in the companion paper (Abdurro'uf & Akiyama 2017), we use eight bands (F435W, F606W, F775W, F814W, F850LP, F125W, F140W and F160W) imaging data from CANDELS (Grogin et al. 2011; Koekemoer et al. 2011) and 3D-HST (Brammer et al. 2012) which cover  $\sim 4000\text{\AA} - 16000\text{\AA}$ . The eight bands at  $z \sim 1$  have similar rest-frame wavelength coverage to the seven bands (FUV, NUV,  $u$ ,  $g$ ,  $r$ ,  $i$  and  $z$ ) of GALEX and SDSS imaging data for galaxies at  $z \sim 0$ . Thanks to the wide wavelength coverage, degeneracy between age and dust extinction (inherent in the stellar population synthesis models) can be broken. The dust extinction can be constrained by the rest-frame FUV-NUV colour (observed F435W-F606W colour at  $z \sim 1$ ), while age can be constrained by the rest-frame  $u - g$  colour (observed F775W-F850LP colour at  $z \sim 1$ ).

We select sample galaxies located in the GOODS-S field from 3D-HST catalog (Skelton et al. 2014; Brammer et al. 2012) based on  $M_*$  and redshift. In the catalog, the  $M_*$  is calculated by  $0.3\mu\text{m}$  to  $8\mu\text{m}$  SED modeling using the FAST code (Kriek et al. 2009) and redshift is determined from three methods: (1) photometric redshifts using  $0.3\mu\text{m}$  to  $8\mu\text{m}$  SED fitting with EAZY code (Brammer et al. 2008), (2) two-dimensional grism spectroscopy by 3D-HST and (3) ground-based spectroscopy. For SFR, we do not use SFR derived by FAST code, instead we use the SFR calculated following Whitaker et al. (2014), which uses the combination of rest-frame UV and IR luminosities. We applied following criteria to select the sample galaxies: (1) redshift range within  $0.8 <$

$z < 1.8$ , (2) stellar mass larger than  $10^{10.5} M_\odot$ , (3) observed in the eight bands, (4) face-on configuration with ellipticity less than 0.6 or  $b/a > 0.4$  and (5) late-type (disc) morphology with Sérsic index ( $n$ ) less than 2.6.

The redshift range is determined to achieve resolution of  $\sim 1$  kpc with F160W image, which has largest full width at half-maximum (FWHM) with 0.19 arcsec among the eight bands. In the redshift range, the eight band coverage samples the rest-frame SED in the FUV to near-infrared (NIR) wavelength. We apply the same mass limit of  $10^{10.5} M_\odot$  as in Abdurro'uf & Akiyama (2017). We select face-on galaxies to minimize the effect of dust extinction. The ellipticities of the galaxies are calculated by averaging the F125W-band elliptical isophotes outside an effective radius, as described in the construction of the radial profiles (see Section 4.2). The Sérsic index is calculated based on Sérsic profile fitting to the one-dimensional stellar mass surface density radial profile ( $\Sigma_*(r)$ ) using the maximum likelihood method. The calculation of  $\Sigma_*(r)$  and the Sérsic index is explained in Section 4.2. In addition to the five selection criteria described above, we only select galaxies which have more than four bins of pixels with a signal-to-noise (S/N) ratio of more than 10 in all of the eight bands (see Section 3.2 of Abdurro'uf & Akiyama (2017) for the description on the binning method).

For galaxies with the photometric redshift, we check the reliability of the redshift estimation by fitting the integrated SEDs of the galaxies in the F435W to F160W bands with the model SEDs, which are calculated at the redshifts of the galaxies. We use a maximum likelihood method to get the best-fitting model SED. We find eight galaxies with a strange SED that results in very large  $\chi^2$  and lead to an unreliable redshift estimate, while the other galaxies have small  $\chi^2$ , which indicates the reliability of their photometric redshifts. We then exclude the eight galaxies from the sample. Finally, we cross-match the remaining 163 galaxies with the *Chandra* 7 Ms sources catalog (Luo et al. 2017; Yang et al. 2017) to remove galaxies with a luminous AGN activity. The *Chandra* catalog contains X-ray sources from the  $\sim 7$  Ms exposure in the *Chandra* Deep Field-South (CDF-S), which covers GOODS-S field. We find 11 galaxies that have a luminous X-ray AGN activity ( $L_{2-10\text{keV}} > 10^{43} \text{ erg s}^{-1}$ ) among the sample. We then exclude those galaxies from the sample to avoid contamination by the contribution from the non-stellar AGN component to the broad band photometry. Finally, 152 galaxies are selected for further analysis. Top panel of Fig. 1 shows the  $M_*$  and SFR of the 152 sample galaxies (blue circles) along with the distribution of entire galaxies more massive than  $10^{9.5} M_\odot$  at  $0.8 < z < 1.8$  in the GOODS-S field (small black circles). The black line indicates global SFMS relation of Speagle et al. (2014) calculated at the median redshift of the sample,  $z = 1.217$ , while the gray shaded area represents  $\pm 0.3$  dex scatter around the global SFMS relation. The purple stars represent AGN-host galaxies. Bottom panel of Fig. 1 shows redshift versus  $M_*$  of the sample galaxies. The figure shows that redshifts of the sample galaxies are spread uniformly within the redshift range.

The eight band mosaic images from the 3D-HST<sup>1</sup> are registered to the same sampling of 0.06 arcsec pixel<sup>-1</sup> and PSF-matched to the F160W image. Background of the mo-

<sup>1</sup> <http://3dhst.research.yale.edu/Data.php>

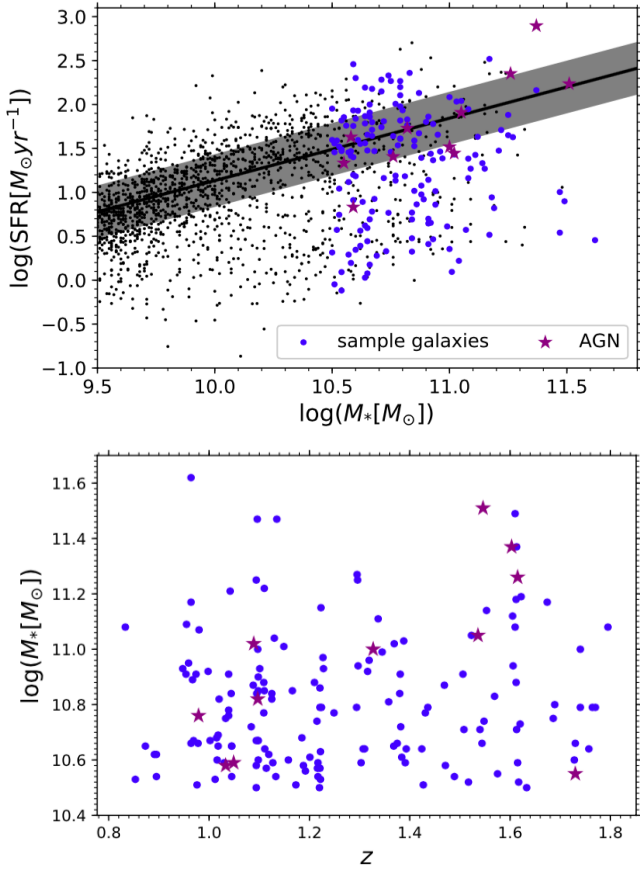


**Figure 1.** Top panel: SFR versus  $M_*$  of galaxies more massive than  $\log(M_*) = 9.5$  at  $0.8 < z < 1.8$  located in the GOODS-S region. Blue circles represent 152 sample galaxies used in this work, while the purple star symbols represent AGN-host galaxies. The black line represents the global SFMS relation of [Speagle et al. \(2014\)](#) calculated at the median redshift of the sample galaxies,  $z = 1.217$ , and the gray shaded area around it represents the  $\pm 0.3$  dex scatter. Bottom panel: redshifts versus  $M_*$  of the sample galaxies.

saic images are subtracted. The FWHM corresponds to the physical scale of  $\sim 1.4 - 1.6$  kpc at  $0.8 < z < 1.8$ .  $5\sigma$  limiting magnitudes of the F435W, F606W, F775W, F814W, F850LP, F125W, F140W and F160W are 27.3, 27.4, 26.9, 27.2, 26.5, 26.1, 25.6 and 26.4 mag within 0.7 arcsec diameter, respectively ([Skelton et al. 2014](#)).

### 3 METHODOLOGY

In order to derive spatially resolved stellar population properties, especially SFR and  $M_*$ , we use a method so-called pixel-to-pixel SED fitting, which is the same method as we used in [Abdurro'uf & Akiyama \(2017\)](#). The methodology is described in detail in [Abdurro'uf & Akiyama \(2017\)](#). We fit spatially resolved SED of each bin with a set of model SEDs using a Bayesian statistics approach. The method can be divided into three main steps: (1) image registration, PSF matching, and pixel binning to get photometric SED of each bin of a galaxy, (2) construction of a library of model pho-

tometric SEDs and (3) fitting the SED of each bin with the set of the model SEDs. Next, we will describe each step.

We do not need image registration and PSF matching because eight bands imaging data provided by the 3D-HST have been registered and PSF-matched as described previously, so the first step is to define an area of a galaxy. To define the area of a galaxy, we firstly generate a segmentation map for the mosaic image of each band using **SEXTRACTOR** ([Bertin & Arnouts 1996](#)) with a detection threshold of above 1.5 times larger than the rms scatter outside of the galaxy, then using the position of a specific galaxy from the 3D-HST catalog, we find the segmentation map around the galaxy. In the **SEXTRACTOR** segmentation map, each object is indicated with a different value, which correspond to the id number of the object in the generated catalog. By reading the pixel value of the galaxy's central pixel and looking for other pixels which have the same value, we can obtain pixels associated with the galaxy. Some outlier pixels which are not connected with the main area of the galaxy are sometimes included in the area of the galaxy, in such case, we exclude those pixels which have no connection to the central pixel of the galaxy. The segmentation maps of the galaxy in eight bands are then merged to define the area of the galaxy.

The next step is converting a pixel value in a unit of count  $s^{-1}$  to the flux in  $\text{erg s}^{-1}\text{cm}^{-2}\text{\AA}^{-1}$  and then pixel binning to increase the S/N ratio. The pixel value to flux conversion is done by multiplying the pixel value with a conversion factor given in the PHOTFLAM header keyword. The pixel binning is done by considering not only an S/N threshold to be reached by combining the pixels, but also similarity of SED shape (tested through  $\chi^2$  calculation) among the pixels which will be binned. The pixel binning is done by first, looking for the brightest pixel in F125W band, then check each neighboring pixel located within a circular annulus centered at the brightest pixel, for the similarity of its SED shape to that SED of the brightest pixel (with  $\chi^2$  below a certain limit) and include the pixel into the bin if its SED shape is similar. Radius of the circular annulus is then increased by 2 pixel and the same procedure is done to add up more pixels until the total S/N of the bin reaches the S/N threshold. Next bin is made by looking for the brightest pixel in the F125W band that was not included in the previous binning and then do the same steps as above. The above procedure is applied until no bin can be made with the remaining pixels. Finally, all the remaining pixels are binned together into one bin. Similar as in [Abdurro'uf & Akiyama \(2017\)](#), we set S/N threshold of 10 in all eight bands and  $\chi^2$  limit of 30. Fig. 2 shows (top panel) the F125W band image and (bottom panel) the binning result of a galaxy GS\_19186, which is located at RA= 53°.120750, DEC= -27°.818984 and  $z = 1.0940$ .

The next step is constructing a library of model SEDs. A library of 300000 model photometric SEDs with a random set of parameters [ $\tau$ ,  $t$ ,  $E(B - V)$ , and  $Z$ ] is generated by interpolating the 286000 parent model SEDs in a grid of those parameters. We use GALAXEV stellar population synthesis model ([Bruzual & Charlot 2003](#)) with [Chabrier \(2003\)](#) initial mass function (IMF) and exponentially declining star formation history of  $\text{SFR}(t) \propto e^{-t/\tau}$ .  $\tau$ ,  $t$ ,  $E(B - V)$ , and  $Z$  represent SFR decaying time scale, age of the stellar population, color excess of dust attenuation, and metallicity of the stellar population, respectively. We multiply parent

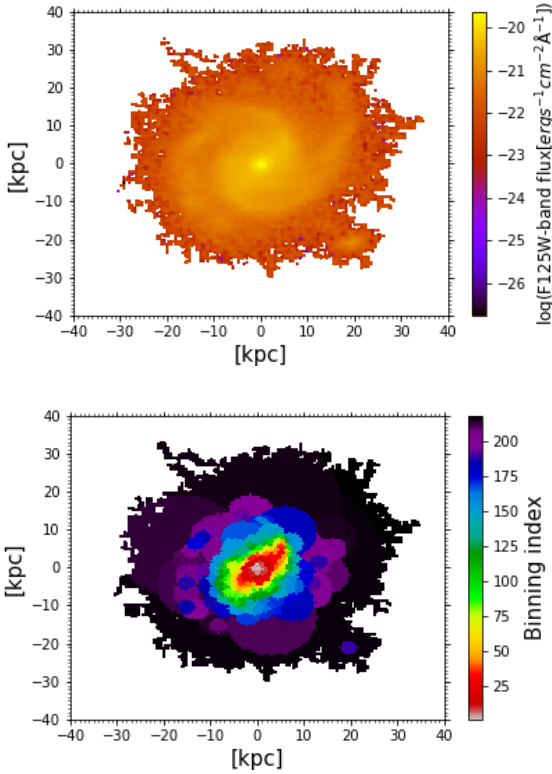


**Figure 2.** Top panel: F125W band image of a galaxy GS\_19186 in the sample which located at RA= 53°.120750, DEC= -27°.818984 and  $z = 1.0940$ . Bottom panel: pixel binning result of the galaxy. Color coding represents index of bin. North is to the top and east is to the left.

model spectra with the eight filter transmission curves of CANDELS and 3D-HST then integrate to get model fluxes in the 8 bands. To apply effect of dust extinction, we use Calzetti et al. (2000) dust extinction law. The random set of parameters have ranges of:  $\tau[0.1 : 10 \text{ Gyr}]$ ,  $t[0.25 : 6.6 \text{ Gyr}]$ ,  $E(B - V)[0 : 0.6 \text{ mag}]$  and  $Z[0.004 : 0.05]$ . Those parameter ranges are the same as those used in Abdurro'uf & Akiyama (2017), except for the age range for which the age of the universe at  $z = 0.8$  is used as an upper limit. As in the previous work, the interpolation to estimate 8 band fluxes and stellar masses for a random parameter set is done in two steps, first interpolation in a three-dimensional space  $[E(B - V), t \text{ and } \tau]$  using a tricubic interpolation for each metallicity, then in one-dimensional space of  $Z$  with a cubic spline interpolation.

After constructing the spatially resolved SED of a galaxy and generating the library of the model SEDs, the next step is fitting the observed SED of each bin with the library of the model SEDs to get  $m_*$  and SFR of the bin. The fitting is done using a Bayesian statistics approach. In this approach, probability distribution functions (PDFs) of the  $m_*$  and SFR are constructed by compounding probabilities of the model SEDs, then posterior means of the  $m_*$  and SFR are calculated. We evaluate probability of a model based on its  $\chi^2$  in a form of Student's  $t$  distribution with degree of freedom,  $\nu$ , of 3, instead of a Gaussian form. It has been verified that, this new model weighting scheme gives a consistent estimate of SFR and sSFR with those estimated

from  $24\mu\text{m}$  flux (see Appendix A of Abdurro'uf & Akiyama (2017)). Uncertainties of the SFR and  $m_*$  are estimated by calculating standard deviation of the PDFs of SFR and  $m_*$ . Once the  $m_*$  and SFR of a bin are obtained, those values are then divided into the pixels that belong to the bin by assuming that the  $m_*$  and SFR of a pixel are proportional to the pixel's fluxes in F160W and F435W bands, respectively.

Fig. 3 shows an example of the pixel-to-pixel SED fitting result for a galaxy GS\_19186 in the sample (whose pixel binning result is shown in Fig. 2). The  $\Sigma_{\text{SFR}}$  map roughly traces spiral arms which are associated with high star formation activity, while the  $\Sigma_*$  map shows smoother distribution. Pixels with negative value in the  $\Sigma_{\text{SFR}}$  ( $\Sigma_*$ ) due to a negative value in the F435W(F160W) flux caused by noise fluctuation, are not shown in the plot with the logarithmic scale. Those pixels with negative values are included in the later analysis e.g. calculation of the integrated SFR and  $M_*$  and radial profiles of  $\Sigma_{\text{SFR}}(r)$  and  $\Sigma_*(r)$ .

Fig. 4 shows the integrated SFR versus  $M_*$  of the sample galaxies (top panel). The integrated SFR and  $M_*$  of a galaxy are derived by summing up the SFR and  $m_*$  of all pixels that belong to the galaxy. In later analysis, we will discuss the difference between spatially resolved SFMS relations of galaxies as a function of their distance from the global SFMS relation in SFR- $M_*$  plane. As we used the global SFMS relation by Speagle et al. (2014) to classify galaxies based on their distance from the global SFMS in Abdurro'uf & Akiyama (2017), here we also use the same global SFMS relation. The solid line in Fig. 4 represents the global SFMS relation calculated at median redshift of the sample,  $z = 1.217$ . The grey-shaded area represents  $\pm 0.3$  dex around the global SFMS relation. Galaxies that are located within  $\pm 0.3$  dex, between  $-0.3$  and  $-0.8$  dex, and below  $-0.8$  dex from the global SFMS are called z1-AMS1 (blue circle), z1-AMS2 (green square), and z1-AMS3 (red diamond), respectively. Numbers of galaxies in the z1-AMS1, z1-AMS2 and z1-AMS3 groups are 47, 72 and 33, respectively.  $UVJ$  diagram in the lower panel of the Fig. 4 shows that the z1-AMS1 galaxies are consistent with star-forming galaxies and majority of the z1-AMS3 galaxies are located within the selection criteria for quiescent galaxies of Williams et al. (2009). The rest-frame colours are taken from the 3D-HST catalog. They are calculated based on the best-fitting spectral template following Brammer et al. (2011).

To check the reliability of our method, especially the SFR estimation, we compare between the integrated SFR derived using our pixel-to-pixel SED fitting method ( $\text{SFR}_{\text{ptpSEDfit}}$ , which is the sum of the SFR of galaxy's pixels) and that from the 3D-HST catalog ( $\text{SFR}_{\text{UV+IR}}$ ) in Fig. 5. It is shown by the figure that the  $\text{SFR}_{\text{ptpSEDfit}}$  is broadly consistent with the  $\text{SFR}_{\text{UV+IR}}$ . The Histogram shows the distribution of the  $\log(\text{SFR}_{\text{UV+IR}}/\text{SFR}_{\text{ptpSEDfit}})$ , which has a mean value ( $\mu$ ) of 0.031 and a standard deviation ( $\sigma$ ) of 0.48 dex. The color-coding represents the ratio of  $\log(\text{SFR}_{\text{UV}}/\text{SFR}_{\text{UV+IR}})$  which is expected to be inversely proportional to the amount of dust extinction. It is shown by the figure that there is a systematic dependence on the amount of dust extinction. It is suggested that the estimated summed SFR from the pixel-to-pixel SED fitting is systematically smaller for galaxies with large dust extinction. However, the effect should not be severe.

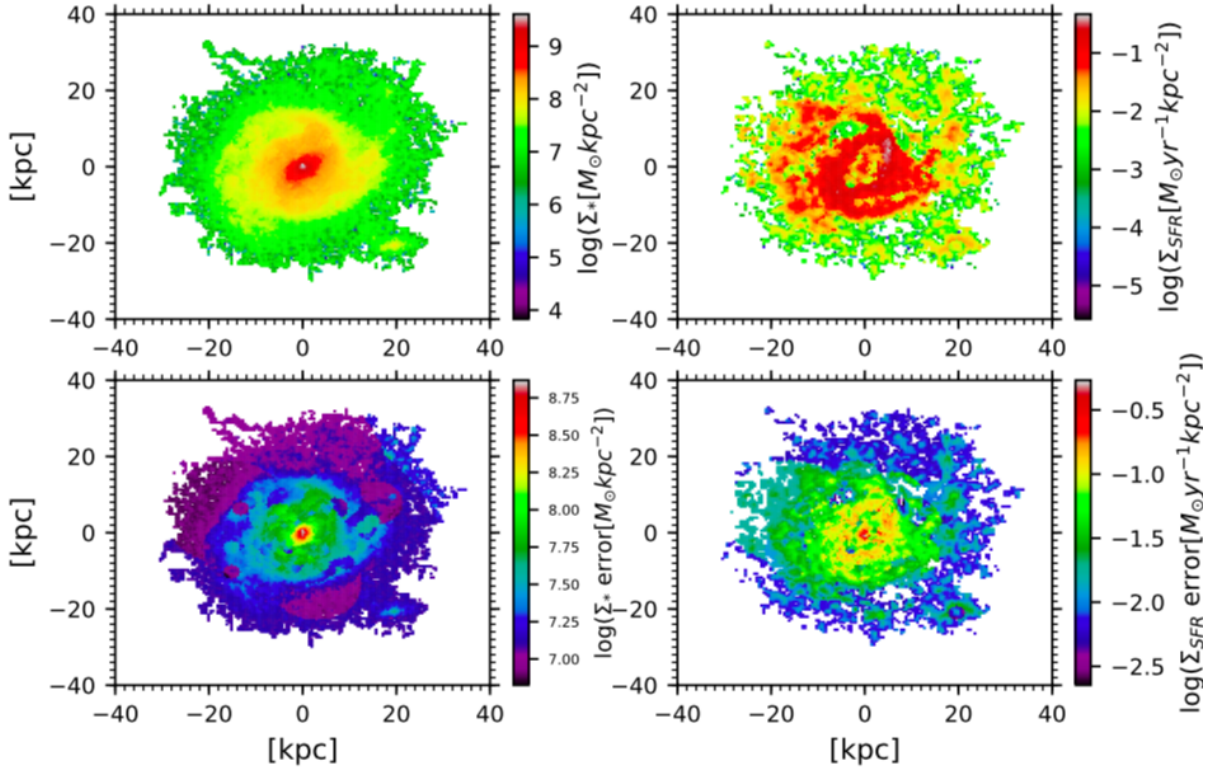


**Figure 3.** An example of pixel-to-pixel SED fitting of a galaxy GS\_19186 (RA= 53°.120750, DEC= −27°.818984 and  $z = 1.0940$ ). Top left panel: stellar mass surface density ( $\Sigma_*$ ) map. Top right panel: SFR surface density ( $\Sigma_{\text{SFR}}$ ) map. Bottom left panel:  $\Sigma_*$  uncertainty map. Bottom right panel:  $\Sigma_{\text{SFR}}$  uncertainty map. Up and left directions correspond to the north and east, respectively.

## 4 RESULTS

### 4.1 Spatially resolved star formation main sequence of massive disc galaxies at $z \sim 1$

To examine the relation between  $\Sigma_*$  and  $\Sigma_{\text{SFR}}$  at  $\sim 1$  kpc scale in the  $z \sim 1$  massive disc galaxies, the  $\Sigma_*$  and  $\Sigma_{\text{SFR}}$  of all 597651 pixels of the sample galaxies are plotted in Fig. 6. In the figure, the contours are colour-coded with the number of pixels in each  $0.1 \times 0.1$  dex bin. The vertical (horizontal) lines at the bottom (left) axes are the median values of  $\Sigma_*$  ( $\Sigma_{\text{SFR}}$ ) for pixels located in the outskirts (the outermost 8 kpc elliptical annulus) of the sample galaxies and they represent the limiting values for those quantities considering the low S/N of the outskirts pixels (S/N  $\sim 0.5$  per pixel). The contours with high number density imply a tight relation between  $\Sigma_*$  and  $\Sigma_{\text{SFR}}$ . The black circles with error bars over-plotted on the contours show the mode of  $\Sigma_{\text{SFR}}$  distribution for each  $\Sigma_*$  bin with 0.3 dex width. Error bars represent the standard deviation from the mode, and calculated separately above and below the mode value. As shown by the mode values, the relation between  $\Sigma_*$  and  $\Sigma_{\text{SFR}}$  is linear at low  $\Sigma_*$  ( $\lesssim 10^{8.5} M_\odot \text{kpc}^{-2}$ ) and flattened at high  $\Sigma_*$  end ( $\gtrsim 10^{8.5} M_\odot \text{kpc}^{-2}$ ).

Fitting the linear part of the mode values (consist of five mode values with  $\Sigma_* \lesssim 10^{8.5} M_\odot \text{kpc}^{-2}$  and excluding the two lowest  $\Sigma_*$  points, which are affected by the limiting value of  $\Sigma_*$ ) with a linear relation with a form of

$$\log \Sigma_{\text{SFR}} = \alpha \log \Sigma_* + \beta \quad (1)$$

using a least-square fitting method resulted in the best-fitting relation with the slope ( $\alpha$ ) of 0.88 and zero-point ( $\beta$ ) of −8.31, which is shown by the black line. The red squares show the spatially resolved SFMS relation of massive ( $\log(M_*/M_\odot) > 10$ ) star-forming galaxies at  $0.7 < z < 1.5$  reported by Wuyts et al. (2013), which was derived from the median of  $\Sigma_{\text{SFR}}$  distribution in each  $\Sigma_*$  bin. They also reported the flattening tendency of the relation at high  $\Sigma_*$  region, although not as clear as the flattening trend obtain in this work. The systematically lower spatially resolved SFMS relation found in this work compared to that reported by Wuyts et al. (2013) is in part caused by the different sample selection; massive star-forming galaxies were used in Wuyts et al. (2013), while in this work, we include not only massive star-forming galaxies but also green-valley and quiescent galaxies which have lower  $\Sigma_{\text{SFR}}$  for a fixed  $\Sigma_*$  at high  $\Sigma_*$  region as will be discussed later.

Next, we investigate the spatially resolved SFMS relation as a function of the distance from the global SFMS. Fig. 7 shows the spatially resolved SFMS relation of z1-AMS1 galaxies (top left, consists of 160210 pixels), z1-AMS2 galaxies (top right, consists of 286721 pixels), z1-AMS3 galaxies (bottom left, consists of 150720 pixels) and the compilation of those three relations (bottom right). The spatially resolved SFMS relations of z1-AMS1, z1-AMS2, and z1-AMS3 are shown with blue circles, green squares, and red triangles, respectively. The spatially resolved SFMS of z1-AMS1 galaxies shows linear increasing trend in the entire  $\Sigma_*$  range, without flattening trend at high  $\Sigma_*$  range as found

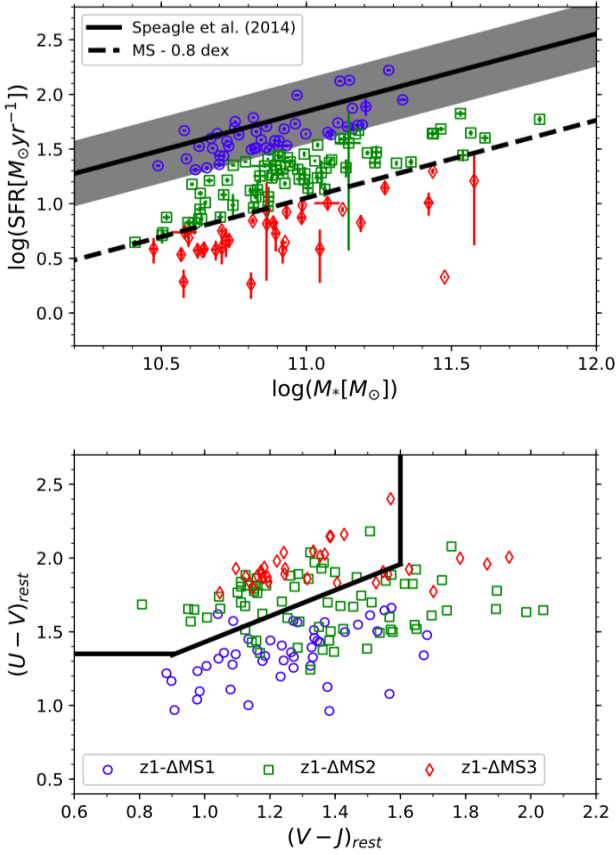


**Figure 4.** Top panel: integrated SFR versus  $M_*$  of the sample galaxies. The solid line represents the global SFMS relation of Speagle et al. (2014) at the median redshift of the sample ( $z = 1.217$ ) and the dashed line represents SFMS-0.8 dex. Grey-shaded region corresponds to  $\pm 0.3$  dex from the global SFMS. The blue circles (located within  $\pm 0.3$  dex about the global SFMS), the green squares (located between  $-0.3$  and  $-0.8$  dex from the global SFMS) and the red diamonds (located below  $-0.8$  dex from the global SFMS) are represent z1-AMS1, z1-AMS2 and z1-AMS3, respectively. Bottom panel: rest-frame  $U - V$  versus  $V - J$  ( $UVJ$  diagram) of the sample galaxies. The upper left 'box' represents the selection criteria for quiescent galaxies by Williams et al. (2009).

in the spatially resolved SFMS for all galaxies (Fig. 6). The flattening at high  $\Sigma_*$  appears in the spatially resolved SFMS of z1-AMS2 galaxies and the flattening is more enhanced in the spatially resolved SFMS of z1-AMS3. The solid line in the top left panel represents the result of a linear function fitting to the eight mode values (excluding one with the lowest  $\Sigma_*$ , which is affected by the  $\Sigma_*$  limit), which has slope of 1.01 and zero-point of  $-9.24$ . The dashed lines in the three panels are the same as the solid line in Fig. 6.

Comparison between the three spatially resolved SFMS relations (bottom right panel) shows similar value of  $\Sigma_{\text{SFR}}$  at the low  $\Sigma_*$  region, while there is a large difference in  $\Sigma_{\text{SFR}}$  at the high  $\Sigma_*$  region. Most of the pixels associated with high  $\Sigma_*$  are located in the central region, while the pixels associated with low  $\Sigma_*$  are located in the disc region. The linear increasing trend of the spatially resolved SFMS of z1-AMS1

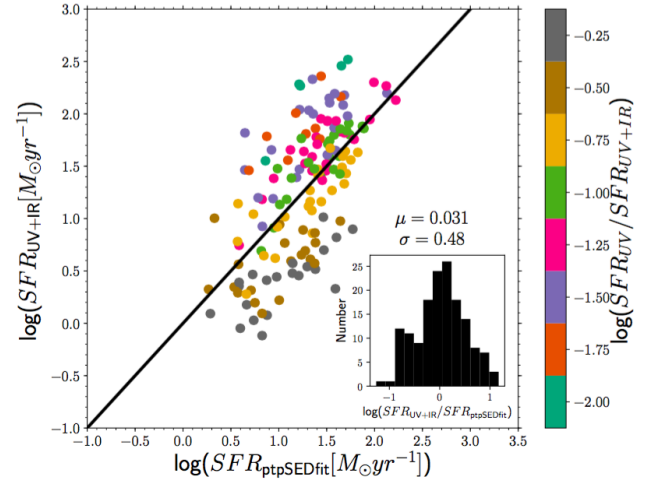


**Figure 5.** Comparison between the integrated SFR estimated using the pixel-to-pixel SED fitting method ( $\text{SFR}_{\text{ptpSEDfit}}$ ) and that from the 3D-HST catalog ( $\text{SFR}_{\text{UV+IR}}$ ). The black line shows proportionality line. The histogram shows the distribution of  $\log(\text{SFR}_{\text{UV+IR}}/\text{SFR}_{\text{ptpSEDfit}})$  which has mean value ( $\mu$ ) of 0.031 and standard deviation ( $\sigma$ ) of 0.48 dex. The color-coding represents the ratio of  $\log(\text{SFR}_{\text{UV}}/\text{SFR}_{\text{UV+IR}})$ , which is inversely proportional to the amount of dust extinction.

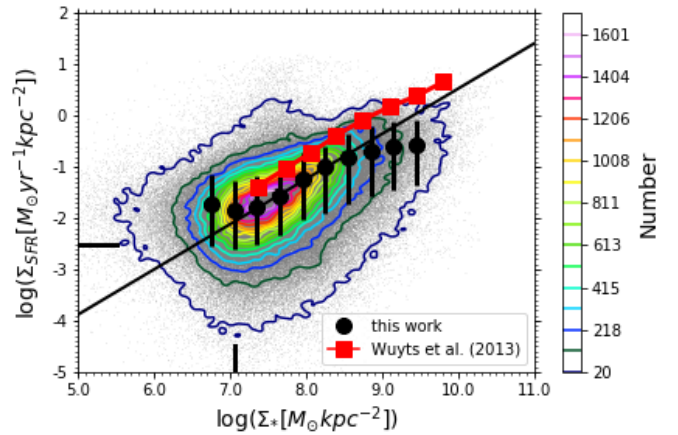


**Figure 6.**  $\Sigma_{\text{SFR}}$  versus  $\Sigma_*$  of all 597651 pixels of the 152 sample galaxies shown with contours colour-coded by number in each  $0.1 \times 0.1$  dex bin. The vertical (horizontal) lines at bottom (left) axes are the limiting values of  $\Sigma_*$  ( $\Sigma_{\text{SFR}}$ ) which are the median values of  $\Sigma_*$  ( $\Sigma_{\text{SFR}}$ ) for pixels located in the outskirts (the outermost 8 kpc elliptical annulus) of the sample galaxies. The black circles with error bars show spatially resolved SFMS relation obtained by taking mode of  $\Sigma_{\text{SFR}}$  distribution for each  $\Sigma_*$  bin with  $0.3$  dex width. The black line represents linear function fitting to the five mode values with  $\Sigma_* \lesssim 10^{8.5} M_{\odot}\text{kpc}^{-2}$  excluding two mode values in the lowest  $\Sigma_*$ . The red line with squares shows the spatially resolved SFMS relation of Wuyts et al. (2013).

galaxies indicates the ongoing star formation activity in the central region as well as in the outskirts, while flattening at high  $\Sigma_*$  region in the spatially resolved SFMS relations of the other groups indicates that a quenching mechanism is ongoing in the central region.

#### 4.2 Radial profiles of $\Sigma_*(r)$ , $\Sigma_{\text{SFR}}(r)$ and $\text{sSFR}(r)$ at $z \sim 1$

Increasing  $\Sigma_*$  along the x-axis of the spatially resolved SFMS plot (Fig. 6 and Fig. 7) roughly corresponds to a decreasing radius toward the central region of the galaxies because the radial profile of  $\Sigma_*(r)$  is always decreasing from the central region to the outskirts. Therefore, the spatially resolved SFMS might be correlated with the radial profiles of  $\Sigma_*(r)$ ,  $\Sigma_{\text{SFR}}(r)$  and  $\text{sSFR}(r)$ . Here, we derive those radial profiles to study how they correlate with the spatially resolved SFMS and also study how those radial profiles change with the distance of the galaxy from the global SFMS.

First,  $\Sigma_{\text{SFR}}(r)$  and  $\Sigma_*(r)$  profiles are constructed by averaging the  $\Sigma_{\text{SFR}}$  and  $\Sigma_*$  of pixels in each elliptical annulus of radius  $r$ . Then  $\text{sSFR}(r)$  profile is obtained by dividing  $\Sigma_{\text{SFR}}(r)$  with  $\Sigma_*(r)$ . An ellipsoid is determined as follows. First, fitting the elliptical isophotes to the F125W-band image of a galaxy using an `ellipse` command in `IRAF`. Then an average ellipticity and position angle are derived based on the ellipsoids outside of a half-mass radius of the galaxy, which is defined as the length of a semi-major axis that encloses half of the total  $M_*$ . The half-mass radius is calculated based on the ellipsoids with ellipticity and position angle that are determined by averaging the ellipticity and position angle of the entire radius. The radial profile is sampled with a 2 kpc step.

Fig. 8 shows the radial profiles of  $\Sigma_{\text{SFR}}(r)$  (left panel),  $\Sigma_*(r)$  (middle panel) and  $\text{sSFR}(r)$  (right panel). Blue square profile shows an individual radial profile of the sample galaxies, while an average radial profile is shown by green circle profile. The radial profiles are considered up to a semi-major axis of 17 kpc. Before calculating the average radial profile, each radial profile is extrapolated if it does not reach semi-major axis of 17 kpc. The extrapolation is done by fitting the radial profile with an exponential function using a least-square fitting method. The fitting is done in the outer region with semi-major axis larger than 3 kpc to avoid the effect of a bulge component. The extrapolated part of the radial profile is shown with a black line. The error bars in the average radial profiles are calculated using the standard error of mean.

On average, the  $\Sigma_*(r)$  and  $\Sigma_{\text{SFR}}(r)$  of  $z \sim 1$  massive disc galaxies have a peak at the centre and gradually decline toward the outskirts, while the average  $\text{sSFR}(r)$  is almost flat over the entire region. The flat average  $\text{sSFR}(r)$  agrees with the linear form of the spatially resolved SFMS. We do not see a significant central suppression of  $\text{sSFR}$  in the average  $\text{sSFR}(r)$ , though it is expected from the flattening trend of the spatially resolved SFMS at high  $\Sigma_*$ .

Fig. 9 shows the radial profiles of  $\Sigma_{\text{SFR}}(r)$  (left panel),  $\Sigma_*(r)$  (middle panel) and  $\text{sSFR}(r)$  (right panel) as a function of distance from the global SFMS, namely z1-AMS1, z1-AMS2 and z1-AMS3 groups. On average, the z1-AMS1 galaxies have higher  $\Sigma_{\text{SFR}}$  in all radii than the z1-AMS2 galaxies and the z1-AMS2 galaxies have higher  $\Sigma_{\text{SFR}}$  in all radii than

the z1-AMS3 galaxies. The z1-AMS2 and z1-AMS3 galaxies have slightly more concentrated  $\Sigma_*(r)$  with steeper increase toward the central region than the  $\Sigma_*(r)$  of z1-AMS1 galaxies. The  $\text{sSFR}(r)$  of those three groups show systematic difference in the central region, while the difference is smaller in the outskirts. The z1-AMS1 and z1-AMS2 have a  $\text{sSFR}$  difference of 0.61 dex at semi-major axis of 1 kpc, while the z1-AMS1 and z1-AMS3 have the  $\text{sSFR}$  difference of 1.21 dex at the same semi-major axis. The z1-AMS1 and z1-AMS2 have a  $\text{sSFR}$  difference of 0.10 dex at semi-major axis of 17 kpc, while the z1-AMS1 and z1-AMS3 have the  $\text{sSFR}$  difference of 0.35 dex at the same semi-major axis. Sharp central suppression in the  $\text{sSFR}(r)$  is observed among the z1-AMS2 and z1-AMS3 galaxies, while flat  $\text{sSFR}(r)$  profile is observed for the z1-AMS1 galaxies. Those  $\text{sSFR}(r)$  have correlation with the spatially resolved SFMS of the corresponding groups. The flat  $\text{sSFR}(r)$  of the z1-AMS1 agrees with the linear increasing profile of the spatially resolved SFMS of that group, while the central suppression in the  $\text{sSFR}(r)$  of the z1-AMS2 and z1-AMS3 agrees with the flattening trend at high  $\Sigma_*$  region in the spatially resolved SFMS of those groups.

To check whether the central suppression in the  $\text{sSFR}(r)$  profiles of the z1-AMS2 and z1-AMS3 is real and not caused by a bias toward lower  $\text{sSFR}$  due to only a few quiescent galaxies, we plot histograms of the  $\text{sSFR}$  distribution in the central ( $r \leq 4$  kpc), middle ( $4 < r \leq 10$  kpc) and outskirts ( $r > 10$  kpc) regions of the z1-AMS1 (blue), z1-AMS2 (green) and z1-AMS3 (red) in the right panel of Fig. 9. It is shown by the histograms that the  $\text{sSFR}$ s in the central regions of the z1-AMS2 and z1-AMS3 are systematically lower than that in the central region of the z1-AMS1. It is also shown that the  $\text{sSFR}$  in all of those three regions of the z1-AMS1 have a peak at almost the same  $\text{sSFR}$  of  $\sim 10^{-9.2} \text{ yr}^{-1}$ , which agrees with the flat profile of the  $\text{sSFR}(r)$  of z1-AMS1.

To examine the morphological difference between the z1-AMS1, z1-AMS2 and z1-AMS3, we calculate the Sérsic index and concentration index ( $R_{90}/R_{50}$ ) of each galaxy in those groups and check the distributions of those properties for the corresponding groups. Fig. 10 shows the histograms of the distributions of the Sérsic indexes ( $n$ , top panel) and concentration indexes ( $R_{90}/R_{50}$ , bottom panel).  $n$  is calculated by fitting the  $\Sigma_*(r)$  with Sérsic profile,  $\Sigma_*(r) = \Sigma_*(r_0) \exp\left(-\left(\frac{r}{h}\right)^{1/n}\right)$ . First, the exponential function ( $n = 1$ ) fitting is done to get the initial guess for the radial scale length ( $h$ ) and the zero point ( $\Sigma_*(r_0)$ ). Then the random set of  $n$ ,  $h$  and  $\Sigma_*(r_0)$  are generated according to the following parameter ranges:  $n[0.5, 5]$ ,  $\Sigma_*(r_0)[0.1\Sigma_*(r_0, n = 1), 10\Sigma_*(r_0, n = 1)]$  and  $h[1, 10h_{n=1}]$ . The best-fitting Sérsic profile is determined based on the lowest  $\chi^2$  value. The  $R_{50}$  and  $R_{90}$  in the concentration index are calculated with the semi-major axis that enclose 50% and 90% of the total  $M_*$ , respectively. In both panels, histogram with blue solid, green dashed and red dashed dotted lines represent z1-AMS1, z1-AMS2 and z1-AMS3, respectively. The histograms indicate that the z1-AMS3 galaxies typically have higher Sérsic index and concentration index (also higher bulge to total stellar mass ratio, B/T) than the z1-AMS1 galaxies, while the z1-AMS2 galaxies have both quantities in the intermediate between those two groups.

Those results suggest an existence of a bulge component in the z1-AMS2 and z1-AMS3 galaxies, while the z1-AMS1

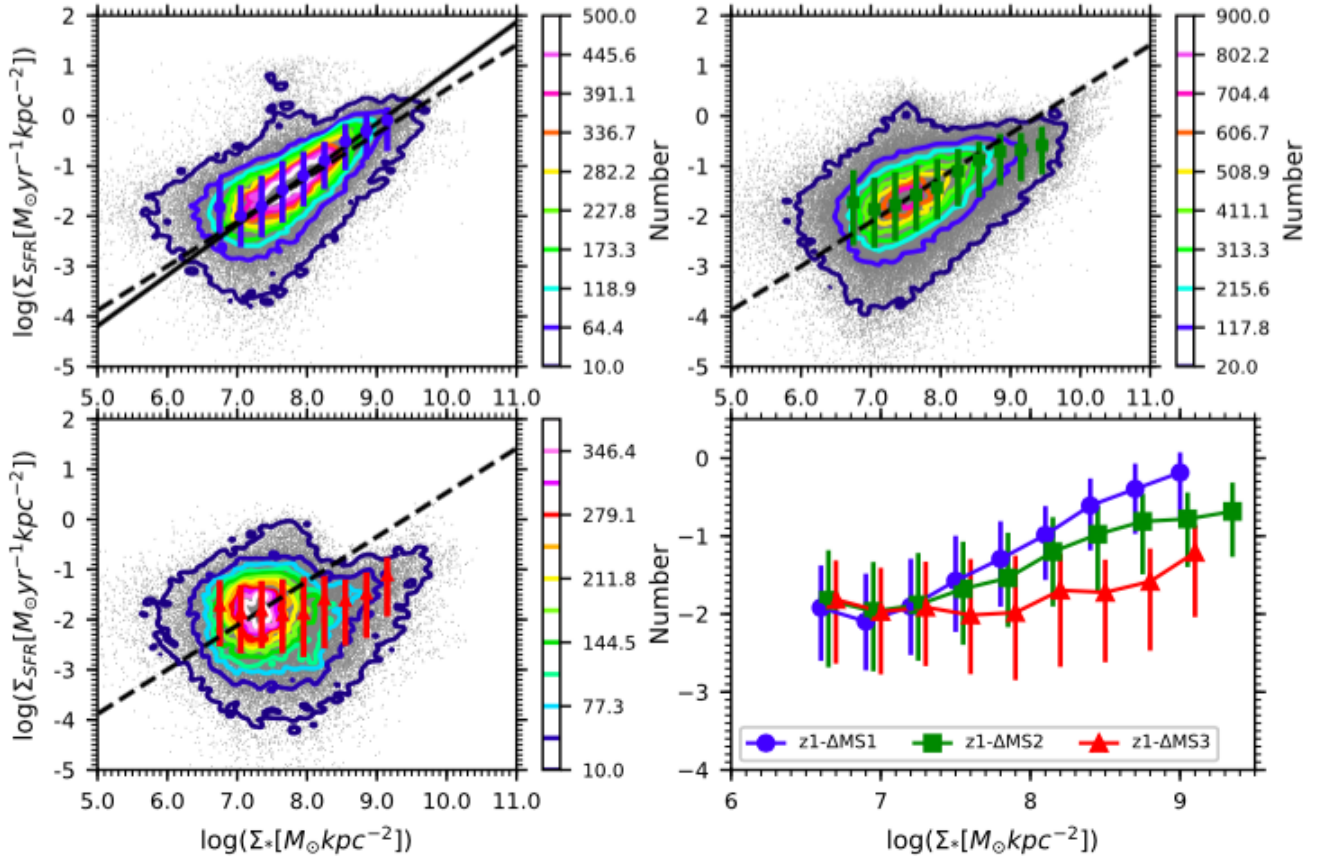


**Figure 7.** Spatially resolved SFMS relations of the galaxies as a function of their distance from the global SFMS. Spatially resolved SFMS relation for galaxies located within  $\pm 0.3$  dex from the global SFMS (z1-ΔMS1; top left panel), between  $-0.3$  dex and  $-0.8$  dex from the global SFMS (z1-ΔMS2; top right panel) and below  $-0.8$  dex from the global SFMS (z1-ΔMS3; bottom left panel). The spatially resolved SFMS relations of z1-ΔMS1, z1-ΔMS2, and z1-ΔMS3 are shown with blue circles, green squares, and red triangles, respectively. The solid line in the top left panel represents the linear function fitting result to the eight mode values (excluding one with the lowest  $\Sigma_*$ ) and the dashed lines in the three panels are the same as the solid line in Fig. 6. Bottom right panel: comparison between the three spatially resolved SFMS relations from the previous three panels. For clarity, blue circles are shifted by 0.05 dex to the left, while red triangles are shifted by 0.05 dex to the right from their actual positions.

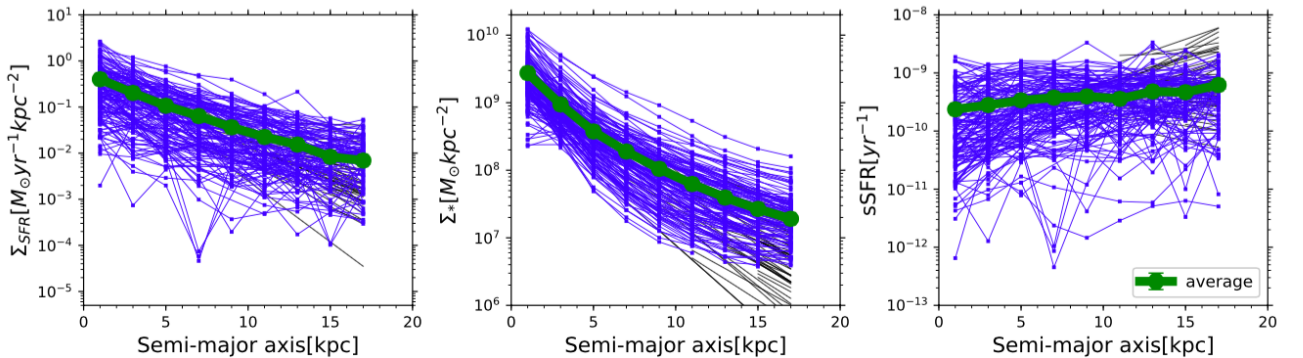


**Figure 8.** Radial profiles of  $\Sigma_{\text{SFR}}(r)$  (left panel),  $\Sigma_*(r)$  (middle panel) and  $s\text{SFR}(r)$  (right panel) of all 152 sample galaxies are shown by blue squares with lines. The radial profiles are cutted up to semi-major axis of 17 kpc. The black lines are the extrapolated part of the radial profiles which are calculated by an exponential function fitting to the region with semi-major axis larger than 3 kpc using a least-square fitting method. The average radial profiles are shown by green circles. Errorbars for the average radial profiles are calculated by standard error of mean.

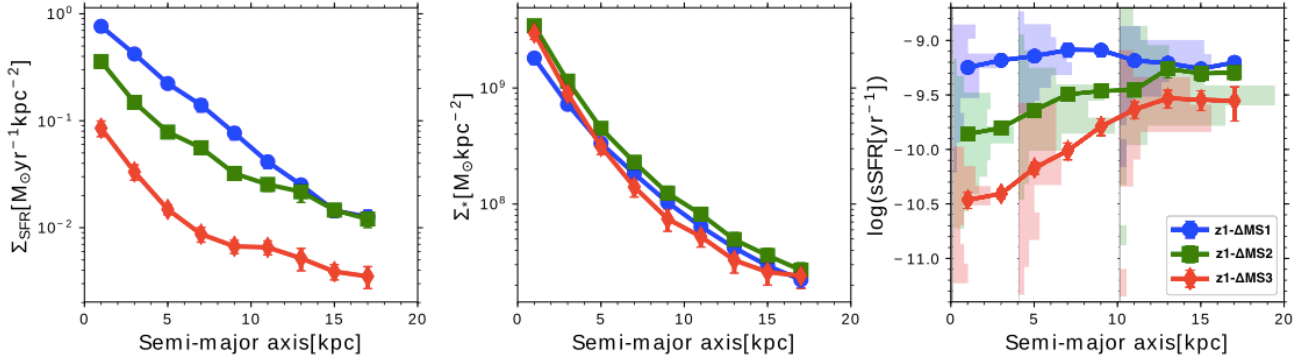


**Figure 9.** Radial profiles of  $\Sigma_{\text{SFR}}(r)$  (left panel),  $\Sigma_*(r)$  (middle panel) and  $\text{sSFR}(r)$  (right panel) as a function of distance from the global SFMS, namely z1-AMS1, z1-AMS2 and z1-AMS3 groups. The radial profiles for z1-AMS1, z1-AMS2 and z1-AMS3 are shown with blue circles, green squares, and red diamonds with line, respectively. Histograms in the right panel show the sSFR distribution in the central ( $r \leq 4$  kpc), middle ( $4 < r \leq 10$  kpc) and outskirt ( $r > 10$  kpc) regions of z1-AMS1 (blue), z1-AMS2 (green) and z1-AMS3 (red) groups.

galaxies are disc-dominated. The flat average  $\text{sSFR}(r)$  profile of the z1-AMS1 suggests that those galaxies are still building their stellar mass in the outskirt as well as in the central region. In Abdurro'uf & Akiyama (2017), we found that the average  $\text{sSFR}(r)$  radial profile of the entire  $z \sim 0$  sample is centrally suppressed. Those observational results agree with the picture of inside-out quenching where galaxies are tend to quench their star formation activity from the central region then the quenching process gradually moves toward the outskirt region. The evidence for the inside-out quenching also reported by previous research papers, e.g. Tacchella et al. (2015), González Delgado et al. (2016), Belfiore et al. (2017), Tacchella et al. (2017).

## 5 DISCUSSION

### 5.1 Spatially resolved SFMS relations of $z \sim 0$ and $z \sim 1$ samples

In order to get insight on the cosmological evolution of the spatially resolved SFMS, we compare the spatially resolved SFMS of the  $z \sim 1$  massive disc galaxies with that of the  $z \sim 0$  massive disc galaxies. The  $z \sim 0$  sample from Abdurro'uf & Akiyama (2017) is based on 93 massive face-on disc galaxies at  $0.01 \leq z \leq 0.02$ . Although our selection criteria for the two samples do not guarantee that the  $z \sim 0$  sample is the descendant of the  $z \sim 1$  sample, it is possible that part of the galaxies from  $z \sim 1$  and  $z \sim 0$  samples are likely to be on the same evolutionary path, i.e. progenitor and descendant. The comoving volumes covered by  $z \sim 1$  and  $z \sim 0$  samples are roughly similar ( $4.5 \times 10^5 \text{Mpc}^3$  and  $4.3 \times 10^5 \text{Mpc}^3$  for  $z \sim 1$  and  $z \sim 0$  samples, respectively). However, the median  $M_*$  of the  $z \sim 1$  sample ( $7.8 \times 10^{10} M_\odot$ ) is systematically higher than that of the  $z \sim 0$  sample ( $3.5 \times 10^{10} M_\odot$ ) and there are 50 massive disc galaxies ( $\log(M_*/M_\odot) \geq 11.0$ ) in the  $z \sim 1$  sample, while only 6 such massive disc galaxies in the  $z \sim 0$  sample. A part of the massive disc galaxies at  $z \sim 1$  are thought to evolve into elliptical galaxies at  $z \sim 0$ . The comoving number density ( $N$ ) and stellar mass density ( $\rho$ ) of  $\log(M_*/M_\odot) \geq 11.0$  disc galaxies in the  $z \sim 1$  sample are comparable to those of the elliptical galaxies

at  $0.01 \leq z \leq 0.02$  (taken from MPA-JHU catalog). The comoving number density and stellar mass density of the  $z \sim 1$  massive disc galaxies are  $\log(N[\text{Mpc}^{-3}]) = -3.9$  and  $\log(\rho[M_\odot \text{Mpc}^{-3}]) = 7.3$ , while those of local elliptical galaxies are  $\log(N[\text{Mpc}^{-3}]) = -4.4$  and  $\log(\rho[M_\odot \text{Mpc}^{-3}]) = 6.7$ , respectively.

We compare the spatially resolved SFMS relations of the six groups in the  $z \sim 1$  and  $z \sim 0$  samples (z1-AMS1, z1-AMS2, z1-AMS3, z0-AMS1, z0-AMS2 and z0-AMS3). The six groups are defined based on the distances from the global SFMS at each redshift. We should emphasize that the classification is based on the order of sSFR at each redshift. In Fig. 11, the six spatially resolved SFMS relations derived from the  $z \sim 0$  and  $z \sim 1$  samples are compared. The shift toward higher  $\Sigma_*$  range for the  $z \sim 1$  sample compared to that for the  $z \sim 0$  sample is caused by the fact that the  $z \sim 1$  sample is systematically more massive than the  $z \sim 0$  sample. An obvious feature shown in Fig. 11 is that the difference in  $\Sigma_{\text{SFR}}$  at a fixed  $\Sigma_*$  between the two spatially resolved SFMS relations at low  $\Sigma_*$  region is small than that at high  $\Sigma_*$  region. If we quantitatively compare the spatially resolved SFMS of galaxies in the highest sSFRs groups, i.e. z1-AMS1 and z0-AMS1, the sSFR difference is 0.4 dex at  $\log(\Sigma_*[M_\odot \text{kpc}^{-2}]) = 7.0$ , while that is 1.5 dex at  $\log(\Sigma_*[M_\odot \text{kpc}^{-2}]) = 8.5$ . This trend suggests that the star formation activity in the disc region (represented with low  $\Sigma_*$  value) shows less suppression from  $z \sim 1$  to  $z \sim 0$  compared to the star formation activity in the central region (represented with high  $\Sigma_*$  value). The trend agrees with the inside-out quenching scenario (e.g. Tacchella et al. 2015; González Delgado et al. 2016; Belfiore et al. 2017; Tacchella et al. 2017).

### 5.2 Empirical model for the evolution of $\Sigma_*(r)$ , $\Sigma_{\text{SFR}}(r)$ and $\text{sSFR}(r)$ radial profiles at $0 \lesssim z \lesssim 1$

We try to construct an empirical evolutionary model of the radial profiles of  $\Sigma_{\text{SFR}}(r)$ ,  $\Sigma_*(r)$  and  $\text{sSFR}(r)$  between  $z = 0-1$ , by defining possible pairs of the progenitor and descendant galaxies from the  $z \sim 1$  and  $z \sim 0$  samples, based on the location on the global SFMS. We define the pairs as follows:

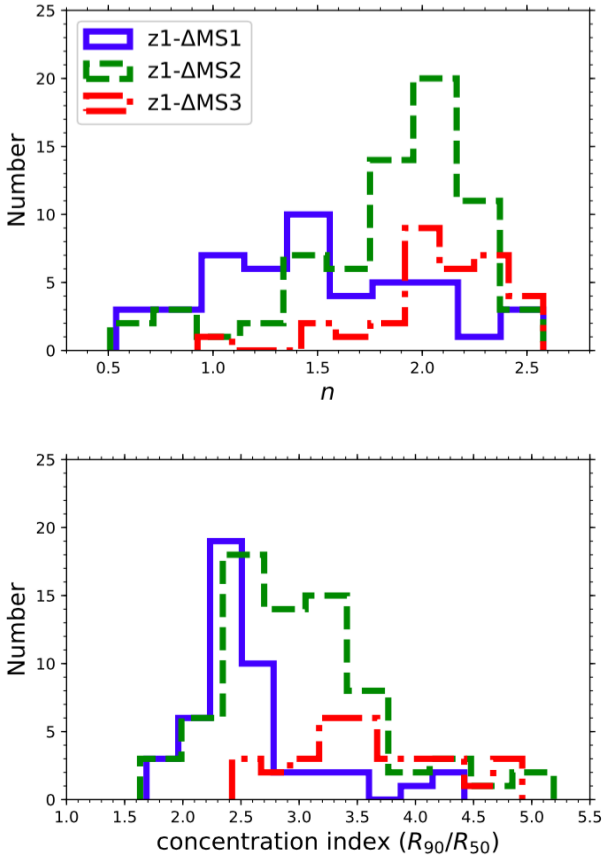


**Figure 10.** Histograms of the distribution of Sérsic indexes ( $n$ , top panel) and concentration indexes ( $R_{90}/R_{50}$ , bottom panel) of z1-AMS1 (blue solid line), z1-AMS2 (green dashed line), and z1-AMS3 (red dashed dotted line).

(1) we start from a galaxy at  $z = 2$  that has sSFR and  $M_*$  within  $\pm 0.3$  dex from the global SFMS relation of [Speagle et al. \(2014\)](#) at that epoch, and use the sSFR and  $M_*$  as a starting point for drawing a galaxy evolutionary track in the  $\log(M_*)$ - $\log(\text{sSFR})$  plane. (2) The star formation history (SFH) of the galaxy is assumed to be in the exponentially declining form,  $\text{SFR}(t) = \text{SFR}(t_0)e^{-\Delta t/\tau}$  with  $t = t_0 + \Delta t$  and  $t_0$  as the age of the universe at  $z = 2$ . (3) We choose a set of model parameters (which are  $M_*(t_0)$ ,  $\text{sSFR}(t_0)$  and  $\tau$ ) which can select as many galaxies as possible from the  $z \sim 1$  and  $z \sim 0$  samples so that the model evolutionary track can be a possible evolutionary path connecting the two samples.

Using the average  $\Sigma_{\text{SFR}}(r)$  of the progenitor and descendant samples selected from the above assumptions, we can infer the radially-resolved SFH, from which we can follow the radial stellar mass buildup during the epoch of  $0 \lesssim z \lesssim 1$ . We consider three different evolutionary paths: two with long and short  $\tau$ , and the other one with just consider a same mass range. To make a model evolutionary track, we assume a certain range for each parameter which produce broad evolutionary track, instead of assuming a single value for each model parameter which only produce an evolutionary track with a single line. The two models with exponentially declining SFH are: (a) model with parameter ranges

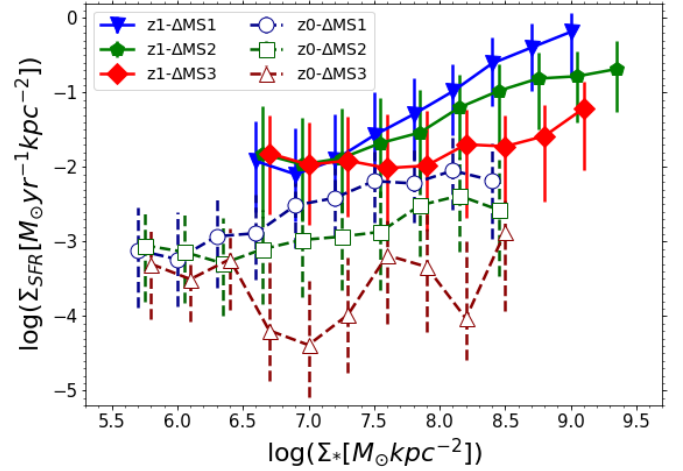


**Figure 11.** Six spatially resolved SFMS relations derived from the  $z \sim 1$  sample (z1-AMS1 (blue solid triangles), z1-AMS2 (green solid pentagons), and z1-AMS3 (red solid diamonds)) and  $z \sim 0$  sample (z0-AMS1 (dark blue open circles), z0-AMS2 (dark green open squares), and z0-AMS3 (dark red open triangles)). The  $z \sim 0$  sample from [Abdurro'uf & Akiyama \(2017\)](#) is based on 93 massive face-on disc galaxies at  $0.01 \leq z \leq 0.02$ . For clarity, blue solid triangles and dark blue open circles are shifted by 0.05 dex to the left, while red solid diamonds and dark red open triangles are shifted by 0.05 dex to the right from their actual positions.

of  $\log(M_*(t_0)) = [9.7 : 9.9]$ ,  $\log(\text{sSFR}(t_0)) = [-8.6 : -8.4]$  and  $\tau = [4.0 : 6.0]$ , hereafter called model A; and (b) model with  $\log(M_*(t_0)) = [10.2 : 10.3]$ ,  $\log(\text{sSFR}(t_0)) = [-8.7 : -8.5]$  and  $\tau = [1.3 : 2.5]$ , hereafter called model B. The  $M_*$ , sSFR and  $\tau$  are in unit of  $M_\odot$ ,  $\text{yr}^{-1}$  and Gyr, respectively. The third model, which is called model C, is made without any assumption on the SFH and only connects galaxies in the stellar mass range of  $10.85 \leq \log(M_*/M_\odot) \leq 11.2$ .

Fig. 12 shows the model evolutionary tracks and the selected progenitor and descendant galaxies for the model A (left panel), B (middle panel) and C (right panel). The black lines represent the model evolutionary tracks if the model parameters are taken from the middle values of the ranges, while the vertical and horizontal gray dashed-lines at each redshift represent the ranges of the sSFR and  $M_*$  if the model parameter ranges are used. The vertical "errorbar" is extended by 0.3 dex above and below from the actual length to make it roughly as wide as the scatter of the global SFMS (which is expected to be able to account for a fluctuations of a real galaxy evolutionary path around the simple exponentially decaying form), while the horizontal "errorbar" is kept as the original length. The scatter in the vertical direction also accounts for the higher uncertainty of the sSFR compared to  $M_*$  of the sample galaxies. The progenitors (descendants) are defined as the galaxies from  $z \sim 1$  ( $z \sim 0$ ) sample which are enclosed within the "box" given by the vertical and horizontal "errorbars", evaluated at the redshifts of the galaxies. Three green boxes show the ranges in sSFR and  $M_*$  given by the horizontal and vertical "errorbars" of the model evolutionary track calculated at  $z = 1.8, 0.8$ , and 0. The number of progenitors (descendants) selected using the model A, B and C are 20(14), 57(6) and

71(14), respectively. As expected from the larger value of  $\tau$ , the sSFR of model A decline more slowly compared to that of model B. The purple dashed line and purple shaded region represent the global SFMS relation at  $z = 2$  and  $\pm 0.3$  dex scatter around it, respectively. The black dashed-lines represent the global SFMS relations at  $z = 1.2$  and  $z = 0.015$ .

Fig. 13 shows the average radial profiles of the selected progenitors (blue circle with solid line) and descendants (red open square with dashed line) galaxies using the evolutionary tracks of the model A (first row), B (second row) and C (third row). The average radial profiles of  $\Sigma_{\text{SFR}}(r)$  and sSFR( $r$ ) show that the star formation activity is declined in all radii from  $z \sim 1$  to  $z \sim 0$  with larger decline in the central region compared to that in the outskirts. The stellar mass buildup in model A shows larger stellar mass increase over all radii compared to that in model B, as expected from the larger  $\tau$  of model A than that of model B. The radial stellar mass increase is not found in model C.

Given the radial decrease of  $\Sigma_{\text{SFR}}(r)$  from  $z \sim 1$  to  $z \sim 0$ , we derive an empirical model for the evolution of the  $\Sigma_{\text{SFR}}(r)$ ,  $\Sigma_*(r)$  and sSFR( $r$ ). Here, we assume exponentially declining SFH at each radius in the form

$$\Sigma_{\text{SFR}}(r, t) = \Sigma_{\text{SFR}}(r, t_0)e^{-\Delta t/\tau(r)} \quad (2)$$

where  $t = t_0 + \Delta t$  with  $t_0$  is the age of the universe at the median redshift of the progenitors. The median redshift of the selected progenitors (descendants) by model A, B and C are  $1.064 \pm 0.026$  ( $0.016 \pm 0.001$ ),  $1.133 \pm 0.043$  ( $0.017 \pm 0.002$ ) and  $1.216 \pm 0.044$  ( $0.017 \pm 0.002$ ), respectively. The uncertainty of the median redshift (which is calculated using bootstrap resampling method) is used in later analysis for calculating the uncertainty of model properties, such as radial profile of SFH,  $\Sigma_*(r)$  and sSFR( $r$ ).

Using Eq. 2 with  $\Delta t$  as the time difference between the median redshifts of the progenitors and descendants ( $7.74 \pm 0.10$ ,  $7.97 \pm 0.17$  and  $8.25 \pm 0.12$  Gyr for model A, B and C, respectively), we calculate the  $\tau(r)$  at each radius. The results for all three models are shown in the left panel in each row of Fig. 14. The  $\tau(r)$  is increasing with increasing radius in all three models. The errorbar at each radius is the  $1\sigma$  uncertainty calculated through Monte-Carlo method, which calculate  $\tau(r)$  randomly by varying the average  $\Sigma_{\text{SFR}}(r)$  of the progenitors and descendants and  $\Delta t$  within their uncertainties following Gaussian distribution. The uncertainty of  $\Delta t$  is calculated using Monte-Carlo method, which calculate  $\Delta t$  randomly by varying the median redshifts of the progenitors and descendants within their uncertainties following Gaussian distribution. The red line in the  $\tau(r)$  plot shows the result of exponential function fitting and the red shaded area shows its  $1\sigma$  uncertainty. They are calculated using a Bayesian statistic method. The middle and right panels in each row show the predicted  $\Sigma_*(r)$  and sSFR( $r$ ) by the model at the median redshift of the descendants (shown with a black line). The predicted  $\Sigma_*(r)$  and sSFR( $r$ ) by the model A and B are consistent with the average radial profiles of the descendants, while those of model C show large discrepancy from the observed radial profiles at  $z \sim 0$ . The consistency suggests that model A and B are possible evolutionary models describing the radial stellar mass accumulation in massive disc galaxies. The simple exponentially declining radial SFH model can explain the stellar mass buildup by the star formation in the massive disc galaxies.

Mathematical descriptions of the evolution of the  $\Sigma_{\text{SFR}}(r)$ ,  $\Sigma_*(r)$  and sSFR( $r$ ) radial profiles are constructed based on the model A. At first, the average  $\Sigma_{\text{SFR}}(r)$  and  $\Sigma_*(r)$  radial profiles of the progenitors are fitted with exponential function and Sérsic profile, respectively, and the best-fitting profiles are used as the initial condition from which the radial profiles at subsequent times are calculated. Those fitting results are

$$\Sigma_{\text{SFR}}(r, t_0) = (0.21 \pm 0.03)e^{-r/(4.18 \pm 0.24)}, \quad (3)$$

$$\Sigma_*(r, t_0) = (8.43 \times 10^9 \pm 4.43 \times 10^8)e^{-(\frac{r}{0.35 \pm 0.02})^{(1.96 \pm 0.03)}}, \quad (4)$$

The time scale of star formation at each radius is determined by an exponential function fitting to the  $\tau(r)$  as

$$\tau(r) = (1.66 \pm 0.22)e^{r/(9.32 \pm 2.21)}, \quad (5)$$

The best-fitting exponential function is shown in the left panel of the first row of Fig. 14 with a red line. The mathematical prescription for the radial profile evolutions are as follows

$$\Sigma_{\text{SFR}}(r, t) = \Sigma_{\text{SFR}}(r, t_0)e^{-(t-t_0)/\tau(r)}, \quad (6)$$

$$\Sigma_*(r, t) = \Sigma_*(r, t_0) + \tau(r)\Sigma_{\text{SFR}}(r, t_0)\left(1 - e^{-(t-t_0)/\tau(r)}\right), \quad (7)$$

where  $t_0$  is the age of the universe at the median redshift of the progenitors and  $t$  is the cosmic time within  $0 \lesssim z \lesssim 1$ . The  $\Sigma_*(r)$  and sSFR( $r$ ) at  $z = 0.8, 0.6, 0.4$  and  $0.2$  calculated based on the above empirical model are shown as gray lines in the middle and right panels of the first row in Fig. 14. The empirical model for the evolution of the  $\Sigma_*(r)$  shows stellar mass buildup in inside-to-outside manner. This inside-out stellar mass buildup in the galaxies is also found by previous researches e.g. van Dokkum et al. (2010); Nelson et al. (2016); Morishita et al. (2015); Tacchella et al. (2015); Tadaki et al. (2017).

We check the consistency between the empirical model of  $\Sigma_{\text{SFR}}(r, t)$  and  $\Sigma_*(r, t)$  radial profiles and the spatially resolved SFMS at  $z \sim 0$  and  $z \sim 1$ . Fig. 15 shows the spatially resolved SFMS relations at redshift interval of  $0.11$  between  $0 \leq z \leq 1.1$  (black circles) constructed from the empirical model of radial profiles. The red lines represent the best-fitting second order polynomial functions to the spatially resolved SFMS constructed from the empirical model. The blue triangles and green squares represent the observed spatially resolved SFMS relations of z1-AMS2 and z0-AMS2 galaxies, respectively. The observed spatially resolved SFMS from those two groups are compared because large fraction of the progenitor and descendant galaxies are belong to those groups. The spatially resolved SFMS relations at  $z = 1.1$  and  $z = 0$  predicted by the empirical model agree with the observed spatially resolved SFMS of z1-AMS2 and z0-AMS2, respectively.

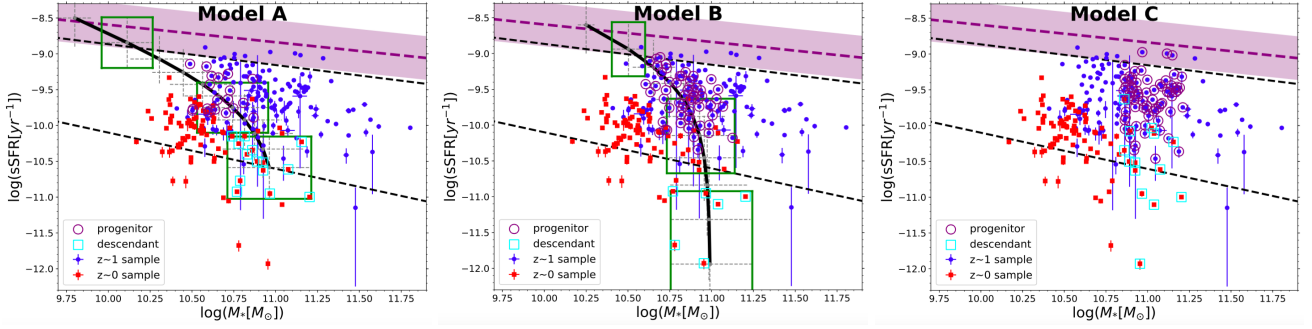


**Figure 12.** Left panel: the evolutionary track and the selected progenitors and descendants of model A which has  $\log(M_*(t_0)) = [9.7 : 9.9]$ ,  $\log(\text{sSFR}(t_0)) = [-8.6 : -8.4]$  and  $\tau = [4.0 : 6.0]$ . Middle panel: the evolutionary track and the selected progenitors and descendants of model B which has  $\log(M_*(t_0)) = [10.2 : 10.3]$ ,  $\log(\text{sSFR}(t_0)) = [-8.7 : -8.5]$  and  $\tau = [1.3 : 2.5]$ . The  $M_*$ , sSFR and  $\tau$  are in unit of  $M_\odot$ ,  $\text{yr}^{-1}$  and Gyr, respectively. The black lines in both panels represent the model evolutionary tracks if the middle value of each model parameter range is used. The gray dashed-line show the range of sSFR and  $M_*$  if the model parameter ranges are considered. Three green boxes show the ranges in sSFR and  $M_*$  given by the horizontal and vertical “errorbars” of the model evolutionary track calculated at  $z = 1.8$ , 0.8, and 0. Right panel: the selected progenitors and descendants of model C which is made without any assumption on the SFH, except the mass range of  $10.85 \leq \log(M_*/M_\odot) \leq 11.2$ . The purple dashed line and purple shaded area represent the global SFMS relation at  $z = 2$  and  $\pm 0.3$  dex scatter around it, respectively. The black dashed-lines represent the global SFMS relations at  $z = 1.2$  and  $z = 0.015$ .

### 5.3 The radial quenching timescale derived from the empirical model

In this section, we estimate the quenching timescale at each radius to quantitatively examine the inside-out quenching process of the sample galaxies. Using the empirical model derived in the previous section, we derive the radial profile of the quenching timescale ( $t_{\text{quench}}(r)$ ). The quenching timescale is the time needed for the sSFR in each radius ( $\Sigma_{\text{SFR}}(r, t)/\Sigma_*(r, t)$ ) to reach a critical value of  $10^{-10} \text{yr}^{-1}$ , which is also used to separate star-forming and quiescent galaxies by Peng et al. (2010) and star-forming and quiescent sub-galactic region by González Delgado et al. (2016), which corresponds to the mass doubling time of 10 Gyr, i.e. larger than the Hubble time at  $z \gtrsim 0.5$ . Black line in Fig. 16 shows  $t_{\text{quench}}(r)$  from  $z = 1.1$ . The gray shaded area around the line represents the  $1\sigma$  uncertainty calculated using the Monte-Carlo method which is done by randomly varying all the parameters involved in the calculation ( $\Sigma_{\text{SFR}}(r, t_0)$ ,  $\Sigma_*(r, t_0)$  and  $\tau(r)$ ) within their uncertainties by assuming Gaussian distribution, then calculate the standard deviation of  $t_{\text{quench}}$  at each radius.

Inside-out quenching process is clearly shown by the  $t_{\text{quench}}(r)$  profile. The  $t_{\text{quench}}(r)$  shows that the central regions ( $r \sim 1$  kpc) will quench by  $\sim 200$  Myr from  $z = 1.1$ , while the outskirts ( $r \sim 15$  kpc) will quench by  $\sim 5.2$  Gyr from  $z = 1.1$ . The model A from which the empirical model is derived has initial mass at  $z = 2$  of  $9.7 \leq \log(M_*/M_\odot) \leq 9.9$  and the progenitor galaxies selected using this model have  $10.5 < \log(M_*/M_\odot) < 10.9$  at  $z \sim 1.1$ . The blue profile in Fig. 16 represents the  $t_{\text{quench}}(r)$  reported by Tacchella et al. (2015) for very massive galaxies with stellar mass range of  $10.8 \leq \log(M_*/M_\odot) < 11.7$ , at  $z \sim 2$ , which has been subtracted by the cosmic time interval between  $z = 1.1$  and  $z = 2.2$ . The  $t_{\text{quench}}(r)$  profile of Tacchella et al. (2015) is derived based on the average  $\Sigma_*(r)$  and  $\Sigma_{\text{SFR}}(r)$  of massive galaxies at  $z \sim 2$  and the average  $\Sigma_*(r)$  of similarly massive early-type galaxies at  $z \sim 0$ . By assuming that the  $z \sim 2$  galaxies keep forming stars with their observed  $\Sigma_{\text{SFR}}(r)$ , they estimated the time needed for each radius to stop their star formation in order not to

overshoot the  $\Sigma_*(r)$  of the  $z \sim 0$  galaxies. By the calculation, they shown that the integrated SFR at any given time is following that of typical main-sequence galaxies.

The blue  $t_{\text{quench}}(r)$  shows the inside-out quenching process of the  $z \sim 2$  massive galaxies, of which the central region is quenched since  $z \sim 2$ , and their star formation is fully quenched in the entire region by  $z \sim 1$ . The  $t_{\text{quench}}(r)$  of low mass (this work) and very massive galaxies (Tacchella et al. 2015) are differ in a starting time of the quenching in the central region, while their slopes are similar. Those  $t_{\text{quench}}(r)$  trends agree with the “downsizing” scenario (e.g. Cowie et al. 1996; Juneau et al. 2005) and furthermore suggests that the “downsizing” phenomenon appear even in the spatially resolved properties. The massive galaxies tend to quench faster in all radius than the low mass galaxies. Pérez et al. (2013) also found the indication that the “downsizing” phenomenon is spatially preserved by analyzing the spatially resolved stellar mass assembly history in local galaxies using integral field spectroscopy observation. They found that massive galaxies assemble their stellar mass faster than low mass galaxies in both inner and outer regions.

## 6 SUMMARY

We investigate the relation between local surface density (at the  $\sim 1$  kpc scale) of SFR ( $\Sigma_{\text{SFR}}$ ) and stellar mass ( $\Sigma_*$ ), so-called spatially resolved SFMS, in the massive ( $\log(M_*/M_\odot) > 10.5$ ) face-on disc galaxies at  $0.8 \leq z \leq 1.8$  and located in the GOODS-S region. We also study the radial profiles of  $\Sigma_{\text{SFR}}(r)$ ,  $\Sigma_*(r)$  and sSFR( $r$ ). The effect of the integrated sSFR to the spatially resolved SFMS and the radial profiles of  $\Sigma_{\text{SFR}}(r)$ ,  $\Sigma_*(r)$  and sSFR( $r$ ) are discussed. By employing our previous results for  $z \sim 0$  massive ( $\log(M_*/M_\odot) > 10.5$ ) face-on disc galaxies (Abdurro'uf & Akiyama 2017), we discuss the evolution of the spatially resolved SFMS and the radial profiles of  $\Sigma_{\text{SFR}}(r)$ ,  $\Sigma_*(r)$  and sSFR( $r$ ) during the epoch of  $0 \lesssim z \lesssim 1$ .

To derive the spatially resolved SFR and stellar mass of a galaxy at  $z \sim 1$ , we use a method so-called pixel-to-pixel

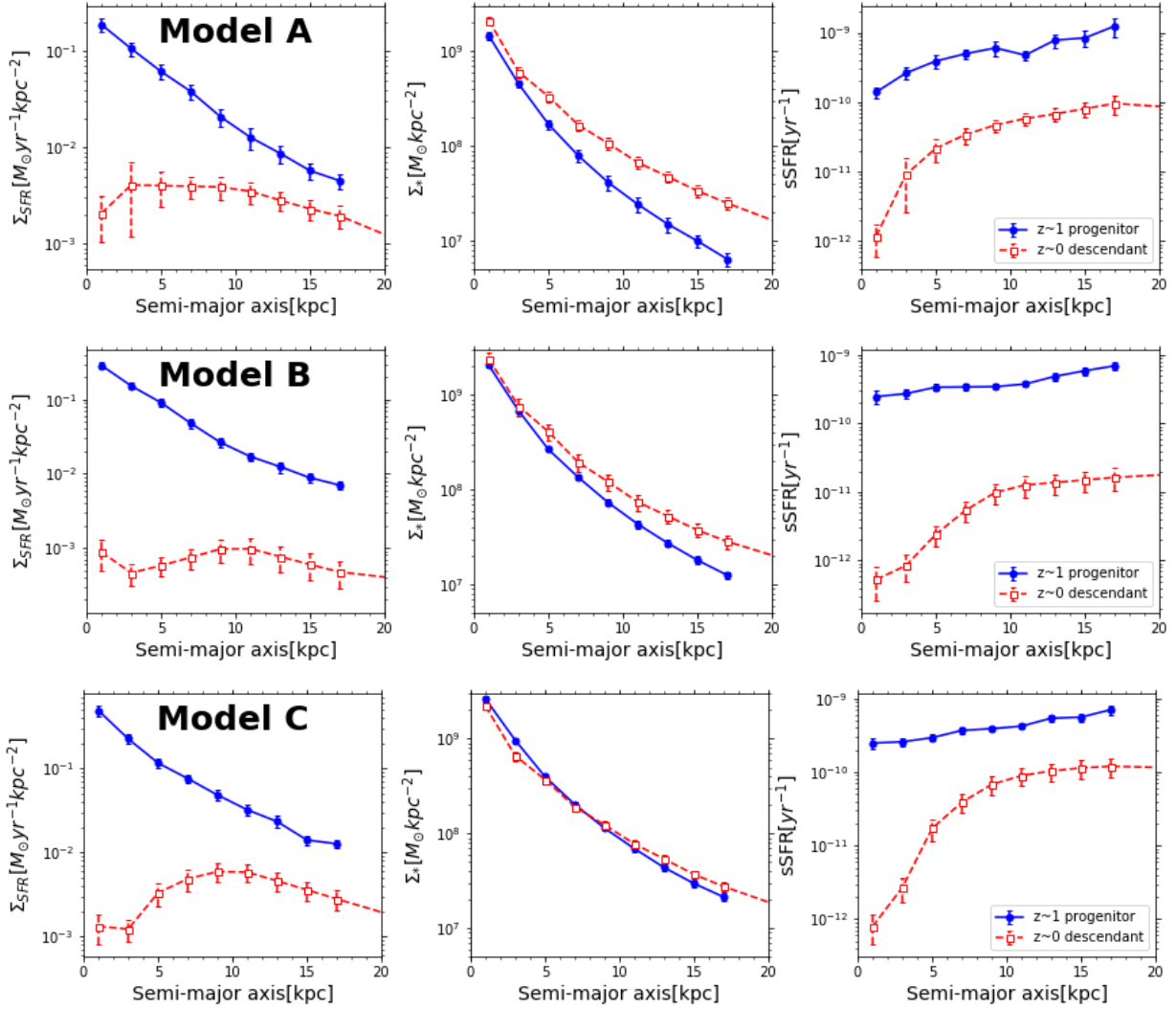


**Figure 13.** Average  $\Sigma_{\text{SFR}}(r)$  (left panel in each row),  $\Sigma_*(r)$  (middle panel in each row) and  $\text{sSFR}(r)$  (right panel in each row) radial profiles of the progenitors (blue circles with solid line) and descendants (red open squares with dashed line) selected by model A (first row), model B (second row) and model C (third row).

SED fitting, which fits the spatially resolved photometric SED in each bin of a galaxy to the library of model photometric SEDs using the Bayesian statistics approach. The spatially resolved SED of a galaxy with rest-frame FUV-NIR coverage is constructed using 8 bands imaging data from CANDELS and 3D-HST.

Our results can be summarized as follows.

1. We find the relation between  $\Sigma_{\text{SFR}}$  and  $\Sigma_*$ , so-called spatially resolved SFMS, in the  $z \sim 1$  sample. This relation has a linear form with the slope of 1.01 in the galaxies which lie within  $\pm 0.3$  dex from the global SFMS (i.e. z1-AMS1), while a flattening trend at high  $\Sigma_*$  end is observed in the spatially resolved SFMS of galaxies which lie between  $-0.3$  and  $-0.8$  dex (i.e. z1-AMS2) and below  $-0.8$  dex (i.e. z1-AMS3) from the global SFMS.
2. The  $\text{sSFR}(r)$  radial profiles of the z1-AMS2 and z1-AMS3 galaxies show decline in the central region, while  $\text{sSFR}(r)$  radial profile of the z1-AMS1 is flat

over the entire radius. The central suppression in the  $\text{sSFR}(r)$  radial profiles of the z1-AMS2 and z1-AMS3 corresponds to the flattening at high  $\Sigma_*$  end of the spatially resolved SFMS of the corresponding groups. The morphology of the z1-AMS3 galaxies show higher Sérsic index and concentration index ( $R_{90}/R_{50}$ ) compared to those of the z1-AMS1, while those values for the z1-AMS2 galaxies are in the intermediate between those two groups. This trend suggests the existence of central bulge components in the z1-AMS2 and z1-AMS3 galaxies, while z1-AMS1 galaxies are disc-dominated system and still building their stellar mass in both of the central region and outskirts.

3. The spatially resolved SFMS shows smaller decline in the low  $\Sigma_*$  region than that in the high  $\Sigma_*$  region from  $z \sim 1$  to  $z \sim 0$ . This trend suggests that the star formation activity in the disc region experienced less suppression compared to the star formation activity in the central region during that epoch, agrees with the inside-out quenching scenario.

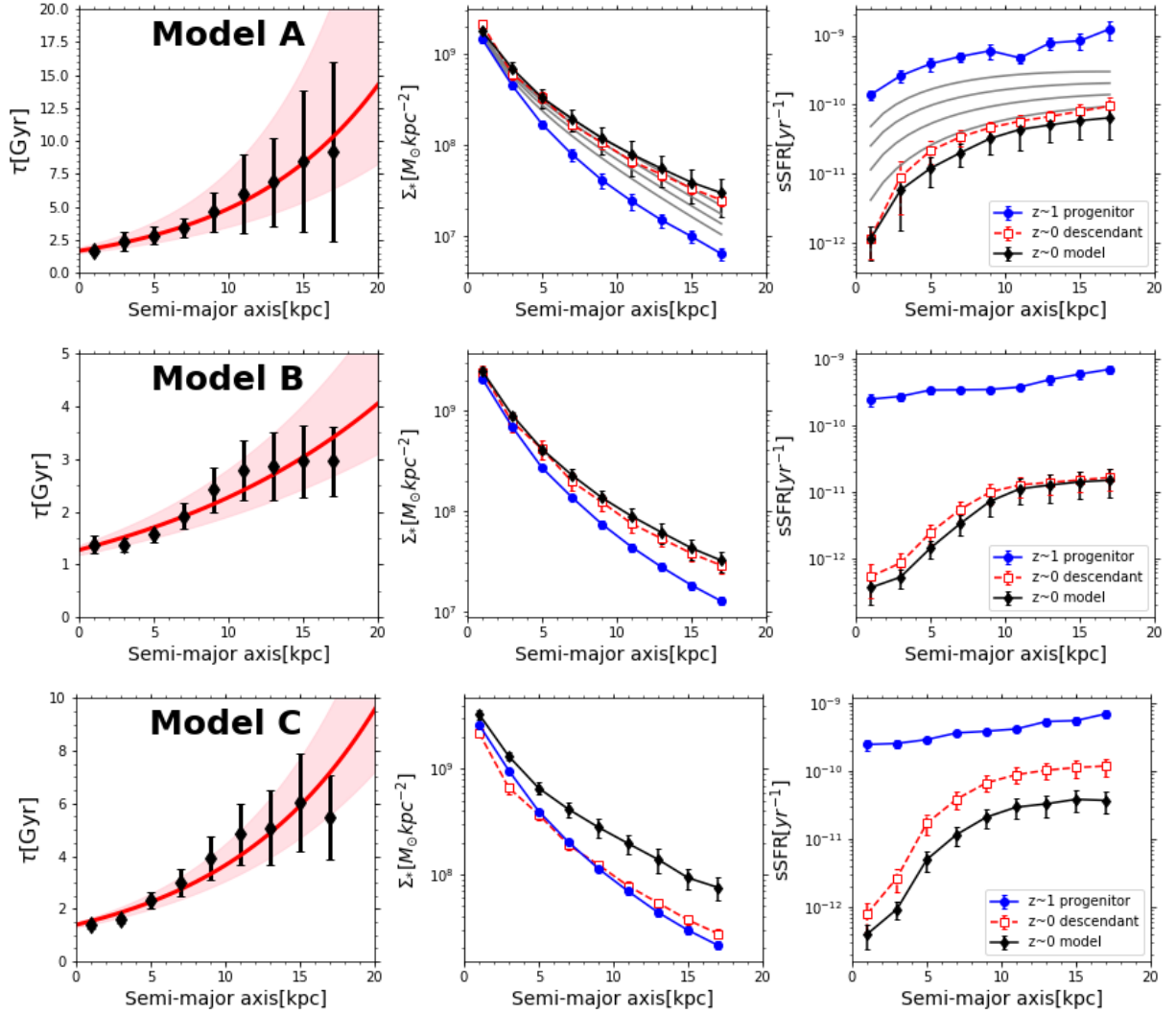


**Figure 14.** Comparison between average  $\Sigma_*(r)$  and  $sSFR(r)$  radial profiles of descendant galaxies and those radial profiles predicted by the empirical models at  $z \sim 0$ . The first, second, and third rows show the radial profile of  $\tau(r)$  (left panel in each row), the observed and predicted radial profiles of  $\Sigma_*(r)$  (middle panel in each row) and the observed and predicted radial profiles of  $sSFR(r)$  (right panel in each row) for model A, B and C, respectively. The black diamonds in the left panel in each row show the  $\tau(r)$  of each model, while the red line and red-shaded region around it show the best-fitting exponential function of the  $\tau(r)$  and its  $1\sigma$  uncertainty, respectively. The  $\Sigma_*(r)$  and  $sSFR(r)$  for progenitor, descendant, and model prediction are shown with blue closed circles with solid line, red open squares with dashed line, and black diamonds with solid line, respectively.

- By selecting pairs of possible progenitors and descendants from the  $z \sim 1$  and  $z \sim 0$  samples using model evolutionary track with exponentially declining SFH, and using the average  $\Sigma_{SFR}(r)$  of the progenitor and descendant galaxies to obtain the radially-resolved SFH following exponentially declining form, we derive the empirical model for the evolution of the  $\Sigma_{SFR}(r)$ ,  $\Sigma_*(r)$  and  $sSFR(r)$  radial profiles. The empirical model successfully reproduce the observed  $\Sigma_*(r)$  and  $sSFR(r)$  radial profiles at  $z \sim 0$  and also consistent with the spatially resolved SFMS at  $z \sim 1$  and  $z \sim 0$ .
- Using the empirical model for the evolution of the  $\Sigma_{SFR}(r)$  and  $\Sigma_*(r)$ , we estimate the radial profile of the quenching timescale.  $t_{\text{quench}}(r)$  is increasing with increasing radius which shows an inside-out progression of the quenching process of the sample galaxies.

The quenching time at each radius is later than that reported by Tacchella et al. (2015) for more massive galaxies. This result suggests that “downsizing” signal is spatially preserved i.e. faster quenching of massive galaxies than low mass galaxies in the entire radius.

## ACKNOWLEDGEMENTS

We thanks Drs. Takahiro Morishita and Sandro Tacchella for their useful comments. We thanks Dr. Sandro Tacchella for providing the radial profile of quenching timescale of massive galaxies at  $z \sim 2$ . Abdurro’uf acknowledges the support from Japanese Government (MEXT) scholarship for his studies.

This work is based on observations taken by the 3D-HST Treasury Program (GO 12177 and 12328) with the

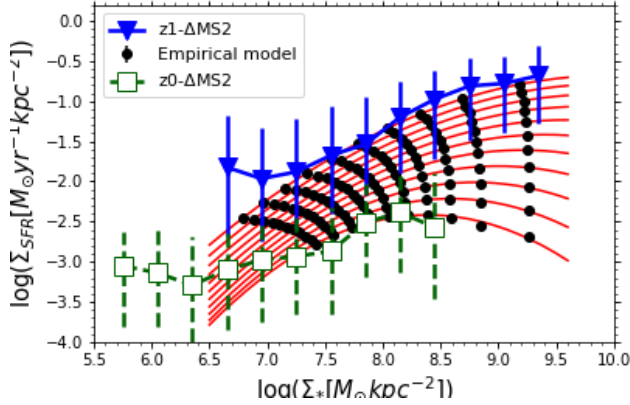


**Figure 15.** Evolution of the spatially resolved SFMS relation as a function of redshift inferred by the empirical model of  $\Sigma_{\text{SFR}}(r)$  and  $\Sigma_*(r)$  radial profiles. The spatially resolved SFMS relations at 0.11 redshift steps between  $z = 0$  and  $z = 1.1$  constructed using the empirical model are shown with black circles. The red line on each spatially resolved SFMS represents best-fitting second order polynomial function. The blue triangles with solid line and green squares with dashed line represent observed spatially resolved SFMS of z1-ΔMS2 and z0-ΔMS2, respectively.

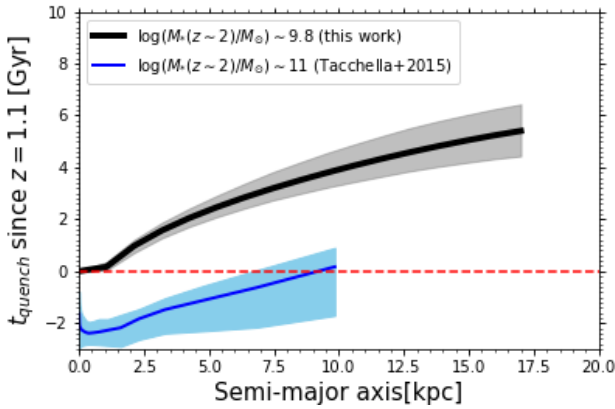


**Figure 16.** Radial profile of the quenching timescale ( $t_{\text{quench}}(r)$ ) from the age of the universe at  $z = 1.1$ . Negative time corresponds to the cosmic time at  $z > 1.1$ . The black line represents  $t_{\text{quench}}(r)$  obtained from this work for  $10.5 < \log(M_*/M_\odot) < 10.9$  galaxies at  $z = 1.1$ , which corresponds to the low-mass galaxies ( $9.7 \lesssim \log(M_*/M_\odot) \lesssim 9.9$ ) at  $z = 2$  (according to model A, see Section 5.2). The blue line represents  $t_{\text{quench}}(r)$  profile reported by Tacchella et al. (2015) for massive galaxies, with stellar mass range of  $10.8 \leq \log(M_*/M_\odot) < 11.7$  at  $z \sim 2$ .

NASA/ESA HST, which is operated by the Association of Universities for Research in Astronomy, Inc., under NASA contract NAS5-26555. This work is based on observations taken by the CANDELS Multi-Cycle Treasury Program with the NASA/ESA HST, which is operated by the Association of Universities for Research in Astronomy, Inc., under NASA contract NAS5-26555.

This work is based on observations made with the

NASA *Galaxy Evolution Explorer*. GALEX is operated for NASA by the California Institute of Technology under NASA contract NAS5-98034. This work has made use of SDSS data. Funding for the Sloan Digital Sky Survey IV has been provided by the Alfred P. Sloan Foundation, the U.S. Department of Energy Office of Science, and the Participating Institutions. SDSS-IV acknowledges support and resources from the Center for High-Performance Computing at the University of Utah. The SDSS web site is [www.sdss.org](http://www.sdss.org). SDSS is managed by the Astrophysical Research Consortium for the Participating Institutions of the SDSS Collaboration including the Brazilian Participation Group, the Carnegie Institution for Science, Carnegie Mellon University, the Chilean Participation Group, the French Participation Group, Harvard-Smithsonian Center for Astrophysics, Instituto de Astrofísica de Canarias, The Johns Hopkins University, Kavli Institute for the Physics and Mathematics of the Universe (IPMU) / University of Tokyo, Lawrence Berkeley National Laboratory, Leibniz Institut für Astrophysik Potsdam (AIP), Max-Planck-Institut für Astronomie (MPIA Heidelberg), Max-Planck-Institut für Astrophysik (MPA Garching), Max-Planck-Institut für Extraterrestrische Physik (MPE), National Astronomical Observatories of China, New Mexico State University, New York University, University of Notre Dame, Observatório Nacional / MCTI, The Ohio State University, Pennsylvania State University, Shanghai Astronomical Observatory, United Kingdom Participation Group, Universidad Nacional Autónoma de México, University of Arizona, University of Colorado Boulder, University of Oxford, University of Portsmouth, University of Utah, University of Virginia, University of Washington, University of Wisconsin, Vanderbilt University, and Yale University.

## REFERENCES

- Abdurro'uf Akiyama M., 2017, *MNRAS*, **469**, 2806  
 Abramson L. E., Morishita T., 2016, preprint, ([arXiv:1608.07577](https://arxiv.org/abs/1608.07577))  
 Belfiore F., et al., 2017, *MNRAS*, **466**, 2570  
 Bertin E., Arnouts S., 1996, *A&AS*, **117**, 393  
 Birnboim Y., Dekel A., 2003, *MNRAS*, **345**, 349  
 Brammer G. B., van Dokkum P. G., Coppi P., 2008, *ApJ*, **686**, 1503  
 Brammer G. B., et al., 2011, *ApJ*, **739**, 24  
 Brammer G. B., et al., 2012, *ApJ*, **753**, 13  
 Brinchmann J., Charlot S., White S. D. M., Tremonti C., Kauffmann G., Heckman T., Brinkmann J., 2004, *MNRAS*, **351**, 1151  
 Bruzual G., Charlot S., 2003, *MNRAS*, **344**, 1000  
 Calzetti D., Armus L., Bohlin R. C., Kinney A. L., Koornneef J., Storchi-Bergmann T., 2000, *ApJ*, **533**, 682  
 Cano-Díaz M., et al., 2016, *ApJ*, **821**, L26  
 Chabrier G., 2003, *PASP*, **115**, 763  
 Cowie L. L., Songaila A., Hu E. M., Cohen J. G., 1996, *AJ*, **112**, 839  
 Daddi E., et al., 2007, *ApJ*, **670**, 156  
 Dekel A., Birnboim Y., 2006, *MNRAS*, **368**, 2  
 Elbaz D., et al., 2007, *A&A*, **468**, 33  
 Fabian A. C., 2012, *ARA&A*, **50**, 455  
 Förster Schreiber N. M., Shapley A. E., Erb D. K., Genzel R., Steidel C. C., Bouché N., Cresci G., Davies R., 2011, *ApJ*, **731**, 65  
 Genzel R., et al., 2014, *ApJ*, **785**, 75

- González Delgado R. M., et al., 2016, *A&A*, **590**, A44
- Grogin N. A., et al., 2011, *ApJS*, **197**, 35
- Hopkins P. F., Hernquist L., Cox T. J., Di Matteo T., Robertson B., Springel V., 2006, *ApJS*, **163**, 1
- Hopkins P. F., Cox T. J., Kereš D., Hernquist L., 2008, *ApJS*, **175**, 390
- Juneau S., et al., 2005, *ApJ*, **619**, L135
- Kauffmann G., et al., 2003, *MNRAS*, **346**, 1055
- Koekemoer A. M., et al., 2011, *ApJS*, **197**, 36
- Kriek M., van Dokkum P. G., Labbé I., Franx M., Illingworth G. D., Marchesini D., Quadri R. F., 2009, *ApJ*, **700**, 221
- Kurczynski P., et al., 2016, *ApJ*, **820**, L1
- Luo B., et al., 2017, *ApJS*, **228**, 2
- Magdis G. E., et al., 2016, *MNRAS*, **456**, 4533
- Maragkoudakis A., Zezas A., Ashby M. L. N., Willner S. P., 2017, *MNRAS*, **466**, 1192
- Martig M., Bournaud F., Teyssier R., Dekel A., 2009, *ApJ*, **707**, 250
- Morishita T., Ichikawa T., Noguchi M., Akiyama M., Patel S. G., Kajisawa M., Obata T., 2015, *ApJ*, **805**, 34
- Murray N., Quataert E., Thompson T. A., 2005, *ApJ*, **618**, 569
- Nelson E. J., et al., 2012, *ApJ*, **747**, L28
- Nelson E. J., et al., 2016, *ApJ*, **828**, 27
- Noeske K. G., et al., 2007, *ApJ*, **660**, L43
- Patel S. G., et al., 2013, *ApJ*, **766**, 15
- Peng Y.-j., et al., 2010, *ApJ*, **721**, 193
- Pérez E., et al., 2013, *ApJ*, **764**, L1
- Salim S., et al., 2007, *ApJS*, **173**, 267
- Sanders D. B., Soifer B. T., Elias J. H., Madore B. F., Matthews K., Neugebauer G., Scoville N. Z., 1988, *ApJ*, **325**, 74
- Schawinski K., et al., 2006, *Nature*, **442**, 888
- Silk J., Rees M. J., 1998, *A&A*, **331**, L1
- Skelton R. E., et al., 2014, *ApJS*, **214**, 24
- Speagle J. S., Steinhardt C. L., Capak P. L., Silverman J. D., 2014, *ApJS*, **214**, 15
- Springel V., Di Matteo T., Hernquist L., 2005, *MNRAS*, **361**, 776
- Tacchella S., et al., 2015, *Science*, **348**, 314
- Tacchella S., Dekel A., Carollo C. M., Ceverino D., DeGraf C., Lapiner S., Mandelker N., Primack Joel R., 2016a, *MNRAS*, **457**, 2790
- Tacchella S., Dekel A., Carollo C. M., Ceverino D., DeGraf C., Lapiner S., Mandelker N., Primack J. R., 2016b, *MNRAS*, **458**, 242
- Tacchella S., et al., 2017, preprint, ([arXiv:1704.00733](https://arxiv.org/abs/1704.00733))
- Tadaki K.-i., et al., 2017, *ApJ*, **834**, 135
- Whitaker K. E., van Dokkum P. G., Brammer G., Franx M., 2012, *ApJ*, **754**, L29
- Whitaker K. E., et al., 2014, *ApJ*, **795**, 104
- Williams R. J., Quadri R. F., Franx M., van Dokkum P., Labbé I., 2009, *ApJ*, **691**, 1879
- Wuyts S., et al., 2011, *ApJ*, **742**, 96
- Wuyts S., et al., 2013, *ApJ*, **779**, 135
- Yang G., et al., 2017, *ApJ*, **842**, 72
- Zolotov A., et al., 2015, *MNRAS*, **450**, 2327
- van Dokkum P. G., et al., 2010, *ApJ*, **709**, 1018

This paper has been typeset from a  $\text{\LaTeX}$  file prepared by the author.